



Progress on the modeling of liquid metal, free surface, MHD flows for fusion liquid walls

N.B. Morley^{a,*}, S. Smolentsev^a, R. Munipalli^b, M.-J. Ni^a, D. Gao^a, M. Abdou^a

^a MAE Department, 43-133 E-IV, University of California, Los Angeles, CA 90095-1597, USA

^b HyPerComp Inc., 31255 Cedar Valley Dr., Suite. 327, Westlake Village, CA 91362, USA

Available online 13 October 2004

Abstract

The proposed use of a flowing liquid metal layers as virtual first-walls for magnetic fusion energy reactors has prompted the development of numerical models capable of predicting the motion of such free surface liquid-metal flows within complex geometry boundaries and in the presence of strong magnetic fields. Several model variants were developed that utilize the assumption of toroidal axisymmetry to simplify the governing Navier–Stokes and Maxwell’s equations to a 2D form. Typically an induced magnetic field formulation has been used to model eddy current formation and various numerical methods and free surface tracking techniques (including height function and volume-of-fluid) have been employed. These axisymmetric models predict a variety of interesting behavior including the effect of toroidal field gradients on the velocity profiles and stability, and the effect of surface-normal magnetic field components on toroidal motion and flow thickness. However, axisymmetric models cannot be used to simulate the true 3D geometry and magnetic field configuration of a magnetic fusion reactor. And so, a 3D, flexible geometry, multiple material, free surface magnetohydrodynamic (MHD) solver called HIMAG has been developed over the past several years. The HIMAG formulation is described in detail along with the results of several initial benchmark problems. Preliminary data from the application of HIMAG to several fusion relevant liquid wall problems including: (1) motion of lithium in a new sample holder for the Divertor Materials Evaluation System (DiMES) experiment on the DIII-D tokamak facility; (2) motion of gallium alloy in a quasi-2D film flow test section in the MTOR facility; (3) motion of gallium alloy in a 3D field film flow test section in the MTOR facility; are also presented and discussed. Finally, future plans for the HIMAG code, including application to the simulation of the effect of insulator coating cracks on closed channel MHD flows, are described.

© 2004 Elsevier B.V. All rights reserved.

Keywords: Free surface; Magnetohydrodynamics; Incompressible; Level-set; APEX

1. Introduction

The APEX project in its first phase examined a large number of first-wall and blanket concepts that had the potential to handle high power density. One class of concepts that seemed particularly promising was that of

* Corresponding author. Tel.: +1 310 206 1230;
fax: +1 310 825 2599.

E-mail address: morley@fusion.ucla.edu (N.B. Morley).

liquid walls. During the initial evaluation of the liquid wall idea, very simplified 1.5D¹ evolution equations for the liquid height were derived from the governing Navier–Stokes and Maxwell’s equations and were used to evaluate the dynamics of liquid-metal flow along a curved first-wall. Both thick liquid metal wall flows, that capture the majority of the neutrons, as well as thin liquid wall flows, where only the surface heat and particle fluxes are captured, were considered as possibilities. There were also ideas advanced as to how externally applied electric currents might aid in controlling the liquid flow by forcing it against the back wall and even providing some measure of in situ pumping by magnetohydrodynamic forces. This work, including a detailed treatment of the flow models, is documented in the APEX Interim Report [1]—a summary of which is available in Abdou et al. [2].

The conclusions of this simple modeling work were that, particularly, thin flowing liquid metal walls (known as *CLiFF* concepts for Convective Liquid Flow First-Wall) appeared feasible within the assumptions of a simple single-component toroidal field and simple cylindrical geometry. Table 1 gives a typical range of thin liquid wall parameters. However, the APEX Interim Report conclusions identified magnetohydrodynamic (MHD) issues in more prototypic fields and geometries as a main feasibility issue that must be seriously addressed by any subsequent research. In particular, the main flow issues were identified as magnetohydrodynamic drag and surface stability effects resulting from:

1. multi-component magnetic fields;
2. strong toroidal and poloidal field gradients;
3. externally applied control currents;
4. 3D geometry, curvature, and penetrations.

Liquid metal MHD modeling research efforts in the second phase of the APEX project have focused mainly on developing the computational capability to investigate these complex free surface LM-MHD issues to a greater degree, and address their impact on the feasibility of the thin liquid metal wall idea. A true resolution of these feasibility issues requires improved modeling where liquid mass, momentum and energy conser-

Table 1

Typical parameter ranges for thin fast-flowing liquid walls and divertors in a fusion power reactor

Quantity (unit)	Symbol	Value
Flow depth (m)	h	0.005–0.04
Flow length (m)	L	1–8
First-wall radius of curvature (m)	R	3–5
Velocity scale (m/s)	U	5–20
Toroidal magnetic field (T)	B	5–15
Toroidal magnetic field gradient (T/m)	∇B	0.25–1.5
Acceleration ($g + U^2/R$) (m/s ²)	g_{eff}	1–130
Kinematic viscosity (m ² /s)	ν	$(0.3–1) \times 10^{-6}$
Electrical conductivity ($\Omega^{-1} \text{m}^{-1}$)	σ	$(2–4) \times 10^6$
Density (kg/m ³)	ρ	500–11000
Surface tension (N/m)	σ_t	0.3–0.6
Magnetic permeability (N/A ²)	μ_m	$\sim 4\pi \times 10^{-7}$
Hartmann number ($Bh(\sigma/\rho\nu)$) ⁵	Ha	500–50,000
Gradient Hartmann number ($\nabla Bh^2/2(\sigma/\rho\nu)$) ⁵	$Ha\nabla$	0.1–100
Reynolds number (Uh/ν)	Re	$10^4–10^6$
Interaction parameter (Ha^2/Re)	N	$10^4–10^5$
Weber number ($\rho U^2 h/\sigma_t$)	We	100–10 ⁵
Magnetic Reynolds number ($\sigma\mu_m Uh$)	Re_m	0.05–1
Froude number (U^2/hg_{eff})	Fr	100–1000

vation, electromagnetics simulation, and free surface tracking capabilities are all accounted for in a much more complete fashion with a minimum of assumptions.

The work reported here can be split into two main efforts: axisymmetric flows, and arbitrary geometry 3D flows. While it was easy to see that a unsteady, fully 3D, arbitrary geometry, free surface LM-MHD flow simulation capability would ultimately be needed to fully address issues of liquid metal wall flows, it was also apparent that the development of such a capability would take several years before even fledgling results could be obtained, and that the parameter ranges accessible by such a *full solution* might be limited. The strategy then was adopted to begin development of a 3D simulation tool while also advancing the simulation capability in reduced dimensions by making use of the approximation of toroidal axisymmetry. In this fashion, we have been continuously increasing our understanding of liquid metal wall flows by modeling more and more complex field and field gradient issues, while working towards the capability needed to simu-

¹ 1.5-D notation is used to denote formulations where the solution has a 2D character, but one of the dimensions is subject to some significant simplification. A similar notation is used for 2.5-D.

late complex geometry flows in 3D. In addition, work in 2D and 2.5D will be used for benchmarking the complex 3D simulation tools. Throughout the paper, the models described all make the assumption of low magnetic Reynolds number $Re_m = \sigma\mu_m Uh \ll 1$,² so that induced magnetic fields are considered small and contributions of the induced fields in electromagnetic body force terms are neglected.

This paper focuses mainly on a description of the modeling development and phenomena observed, while serious application of the models to various design ideas explored in the APEX study is reported elsewhere in this special issue. The subsequent sections are organized to reflect this two-pronged approach to modeling liquid metal walls in strong magnetic fields. Section 2 contains discussion and results of modeling efforts using the axisymmetric approximation, including many results from several different codes using somewhat different numerical procedures. Section 3 contains a description of efforts to develop a fully 3D arbitrary geometry modeling capability as well as initial results to various benchmark and fusion problems. Section 4 will finally summarize important conclusions and direction of ongoing work in this area.

2. Axisymmetric models and simulation results

It is fairly easy to see, given the toroidal geometry of a tokamak, that flows along a first-wall could be idealized such that they extend completely unbroken and without variation in the toroidal direction—around the axis of revolution of a poloidal cross-section. The assumption that the flow, and the magnetic fields through which the flow must move, have no toroidal variation is termed here *axisymmetry*. In general we will use the terms “axisymmetric” and “infinite” in an interchangeable way. In reality axisymmetric flows will have some element of curvature associated with them, but often we will assume that curvature is small and approximate such flows in Cartesian geometry with the x - y plane representing the poloidal plane, and with z coordinate in the toroidal direction. For axisymmetric flows

then we make the assumption that $\partial/\partial z = 0$ to simplify the Navier–Stokes equations:

$$\frac{\partial \mathbf{v}}{\partial t} + (\mathbf{v} \cdot \nabla_{\perp}) \mathbf{v} = -\frac{1}{\rho} \nabla_{\perp} p + \nu \nabla_{\perp}^2 \mathbf{v} + \mathbf{g} + \frac{1}{\rho} \underbrace{(\mathbf{j}_{\perp} \times B_z^0 \hat{z} + j_z \hat{z} \times \mathbf{B}_{\perp}^0)}_{\text{poloidal forces}} + \frac{1}{\rho} \underbrace{\mathbf{j}_{\perp} \times \mathbf{B}_{\perp}^0}_{\text{toroidal forces}}, \quad (1)$$

$$\nabla_{\perp} \cdot \mathbf{v} = 0, \quad (2)$$

where $\mathbf{v} = (u, v, w)$, p , and \mathbf{B}^0 are the velocity, pressure and applied magnetic induction; and ρ , ν , g are the density, kinematic viscosity and acceleration of gravity all assumed constant throughout the working liquid. This formulation keeps all three components of the velocity and applied magnetic field, but no quantity is allowed to vary with z , so that the gradient operator is 2D, $\nabla_{\perp} = (\partial/\partial x, \partial/\partial y, 0)$. We will also use the standard fluid dynamics terminology where streamwise denotes the main flow direction (usually x), transverse denotes the direction transverse to the main flow and normal to the flow substrate (usually y) and spanwise denotes the direction perpendicular to the flow but parallel to the back wall (z -toroidal direction for poloidal flow). The MHD terms in Eq. (1) are separated in such a way to show forces acting in the poloidal plane and forces acting in the toroidal direction.

The convenience of the axisymmetric assumption is that it decouples the effect of magnetic fields applied in the direction of the axisymmetry (toroidal) from those in the poloidal plane. The model of electric currents can be approached most effectively following a hybrid approach, where \mathbf{j}_{\perp} is calculated from a current stream function, and j_z is calculated from Ohm’s law:

$$\mathbf{j}_{\perp} = \frac{1}{\mu_m} \nabla_{\perp} \times B^i \hat{z}, \quad (3a)$$

$$j_z = \sigma(\mathbf{v}_{\perp} \times \mathbf{B}_{\perp}^0), \quad (3b)$$

where B^i is the induced magnetic field (also the stream function for poloidal current), σ the electrical conductivity and μ_m the magnetic permeability of the LM. Eq. (3b) is sufficient for the calculation of j_z since in an axisymmetric 2D flow the electric field drops out, as toroidal currents are able to loop around the entire torus. But an induction type equation is necessary for

² It should be noted that this inequality is not necessarily satisfied in all possible cases described in Table 1.

B^i and can be formulated based on the z -component of the curl of Ohm's law, giving:

$$\frac{1}{\sigma\mu_m}\nabla_{\perp}^2 B^i = (\mathbf{v} \cdot \nabla_{\perp})B_z^0 - (\mathbf{B}^0 \cdot \nabla_{\perp})w \quad (4)$$

Deviations from this standard model (due to toroidal curvature for instance) will be noted as needed.

Some of the modeling effort using the axisymmetric approximation has already been summarized in Morley et al. [3] with details reported in several other journal papers [4–8]. This material will not be described here in detail, but certain features and conclusions of the problems analyzed in these papers will be recounted for completeness, while generally more recent work is highlighted.

2.1. Analytic solutions to special case problems

When focus is placed solely on the effect of variations in the toroidal field, with contributions of other field components neglected $\mathbf{B}^0 = (0, 0, B_z(x, y))$, then there is no source for motion or current in the toroidal direction ($w, j_z = 0$) and the induced magnetic field takes on the form described by

$$\frac{1}{\sigma\mu_m}\nabla_{\perp}^2 B^i = u \frac{\partial B_z^0}{\partial x} + v \frac{\partial B_z^0}{\partial y} \quad (5)$$

What is notable from the form of Eq. (5) is that the behavior of the induced field is governed by standard diffusion with a source term that depends on the spatial (and temporal in a more complete treatment) variations in the applied field. In Cartesian geometry, if there is no variation in the applied field, then there is no MHD effect on the flow in this 2D treatment (aside from laminarization which is implicitly assumed). In other words, the axisymmetric geometry has no Hartmann layers as current closure paths, so that only the effects of the gradients are studied.

It is possible to gain insight into some of the behavior of a free surface flow in a spanwise field with streamwise variation by exploring a special case where $B_z(x, y) = Cx + D$ (where C and D are constants). In this case, with linear field gradient, it is possible to construct an analytic solution to the fully developed flow problem as a function of Hartmann number $Ha_{\nabla} = \nabla B(h^2/2)(\sigma/\rho\nu)^{1/2}$, wherein Ha_{∇} is based on a characteristic field strength calculated from the *gradient* of

B times the characteristic length and not on any local value of the field.

The fully developed solution for the velocity and induced field (electric current) is lengthy and is covered in detail in Ref. [5], but it is readily seen that the resultant mass flow depends only on the gradient value. It is this fact that allows a fully developed solution to be reached at all. Also notable is that the induced current is only streamwise, meaning there are no direct $\mathbf{j} \times \mathbf{B}^0$ retarding forces, only forces acting perpendicular to the main flow direction. These forces create a streamwise pressure gradient that in turn affects the streamwise flow in drastic ways, depending on the strength of the applied field gradient. The velocity profiles for several values of Ha_{∇} are shown in Fig. 1, where at high Ha_{∇} we see the formation of an asymmetric, free surface equivalent of the classic M-shaped velocity profile commonly observed in closed channel flows in gradient fields, with boundary jet thickness scaling with $\sqrt{Ha_{\nabla}}$.

This asymmetric M-shaped velocity is driven purely by the pressure gradient effects, and is the result of the

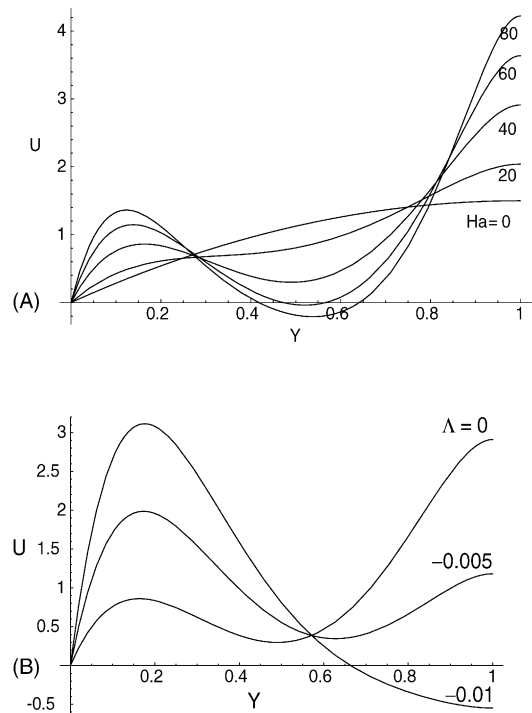


Fig. 1. Fully developed velocity profiles for flow in a linear gradient (A) with applied fields of various strength and (B) with streamwise externally applied current of various strength.

same physical effect as the so-called magnetic propulsion idea [9] proposed to aid in situ pumping of free surface flows in fusion reactors. In the magnetic propulsion scheme, a streamwise applied electrical current is injected into the film flow. This current is oriented such that it pushes the liquid against the supporting wall (which could in theory be inverted to gravity), and due to gradient in the field strength (or the current density itself since the flow cross-sectional area can change) provides a streamwise pressure gradient that propels the flow along. This applied current can be easily added to the preceding analysis through a change in boundary condition on B^i , and gives changes in the velocity profile as shown in Fig. 1. Because the strongest portion of the streamwise pressure gradient is near the back wall, the flow is accelerated predominantly in this region, with relatively slower flow near the surface.

2.2. 2.5D developing flow with height function free surface model and curvature effects

In earlier work during the evolution of the APEX modeling effort the governing equations were formulated based on a Cartesian or cylindrical system. However, the toroidal curvature can be strong especially when considering for example the small radius center-stack of a spherical torus. To address the curvature effects, 3D thin-shear-layer equations for flows of conducting fluids in a magnetic field have been derived in orthogonal body-oriented coordinates and then applied to the analysis of MHD free-surface flows over a curved wall. Unlike the classic boundary-layer-type equations, present ones permit information to be propagated upstream through the induced magnetic field. Another departure from the ordinary hydrodynamic theory is that the normal momentum equation keeps the balance between the pressure gradient term, and those related to gravity, centrifugal forces, and Lorentz force. Thus, the normal pressure variations are allowed. The 3D boundary-layer equations are obtained from the full Navier–Stokes equations (including the Lorentz force term) by neglecting terms which are usually small in the boundary-layer approximation including: the second-order derivatives parallel to the body surface, and all convection and diffusion terms in the surface-normal momentum equation. The simplifications are based on the standard order of magnitude analysis, which does not depart in essence from that for

ordinary flows and is not repeated here. When dealing with the group of the equations for the electromagnetic quantities, the induced currents are allowed to form a closed loop within the flow domain. Therefore unlike the flow equations, all the second derivatives in the induction equations were kept unchanged (a more complete treatment is available in Ref. [10]).

The full model describes basic 3D effects due to the wall curvature and spatial variations of the applied magnetic field. As a particular case, equations for flows with rotational symmetry have been derived and numerical calculations were performed for free-surface flows over a body of revolution under conditions relevant to a fusion reactor. We call this formulation a “2.5D” representation since flow and current in the third (toroidal) direction are included, but variations of quantities in this direction are still not considered. At present this case is of considerable practical importance for fusion applications, where the flow symmetry is allowed by the chamber topology. At the same time this case provides a simplified example of 3D flow in which the variables are independent of the azimuthal angle. Some specific flow patterns, such as flow thickening and spiral-type (strong toroidal motion) flows, have been observed. Of course it should be noted that some 3D features that may be present in the true physical problem, like instabilities with variations in azimuthal angle, are not modeled by such an approach.

Here we will introduce the surface of revolution in a standard way as a surface generated by the rotation of a plane curve around an axis in its plane. The curvilinear body-oriented coordinates of any point in the flow around the surface will be taken as (x, y, θ) . These coordinates form a set of orthogonal coordinates fitted to the surface of the body. Let u, v, w be the components of velocity of the fluid in directions of increasing $x, y,$ and θ respectively. If r is the distance from the axis of revolution to a given point in the liquid, so that r is a function of x alone, then the metric coefficients are, $H_{1,2} = 1,$ and $H_3 = r.$ As for the applied magnetic field, it can be considered to be independent on $y,$ because the dimensions of the body are much larger than the characteristic length scale over which the changes of the applied magnetic field can be significant.

The axisymmetric governing equations using the assumptions and simplifications formulated above are

comprised of three momentum equations:

$$\begin{aligned} \frac{\partial u}{\partial t} + u \frac{\partial u}{\partial x} + v \frac{\partial u}{\partial y} - \frac{w^2}{r} \frac{dr}{dx} \\ = -\frac{1}{\rho} \frac{\partial p}{\partial x} + g_x + v \frac{\partial^2 u}{\partial y^2} + \frac{1}{\rho} (j_y B_\theta^0 - j_\theta B_y^0), \end{aligned} \quad (6a)$$

$$\rho(K_a u^2 + K_b w^2 + g_y) + (j_\theta B_x^0 - j_x B_\theta^0) = \frac{\partial p}{\partial y}, \quad (6b)$$

$$\begin{aligned} \frac{\partial w}{\partial t} + u \frac{\partial w}{\partial x} + v \frac{\partial w}{\partial y} + \frac{uw}{r} \frac{dr}{dx} \\ = g_\theta + v \frac{\partial^2 w}{\partial y^2} + \frac{1}{\rho} (j_x B_y^0 - j_y B_x^0), \end{aligned} \quad (6c)$$

the mass and current continuity equations:

$$\frac{1}{r} \frac{\partial(ru)}{\partial x} + \frac{\partial v}{\partial y} = 0, \quad (7a)$$

$$\frac{1}{r} \frac{\partial(rj_x)}{\partial x} + \frac{\partial j_y}{\partial y} = 0, \quad (7b)$$

the equations of ampere's law and Ohm's law defining the current density:

$$j_x = \frac{1}{\mu_0} \frac{\partial B_\theta^i}{\partial y}, \quad (8a)$$

$$j_y = -\frac{1}{\mu_0} \frac{1}{r} \frac{\partial(rB_\theta^i)}{\partial x}, \quad (8b)$$

$$j_\theta = \sigma(uB_y^0 - vB_x^0) \quad (8c)$$

and the single induction equation for the induced toroidal field:

$$\begin{aligned} \frac{\partial B_\theta^i}{\partial t} = B_x^0 \frac{\partial w}{\partial x} + B_y^0 \frac{\partial w}{\partial y} - \left(\frac{dB_\theta^0}{dx} - \frac{B_\theta^0}{r} \frac{dr}{dx} \right) u \\ - \frac{wB_x^0}{r} \frac{dr}{dx} + \frac{1}{\mu_m \sigma} \left[\frac{1}{r} \frac{\partial}{\partial x} \left(r \frac{\partial B_\theta^i}{\partial x} \right) + \frac{\partial^2 B_\theta^i}{\partial y^2} \right] \\ - \frac{\partial B_\theta^0}{\partial t}. \end{aligned} \quad (9)$$

Here $1/K_a$ and $1/K_b$ are the two principal radii of curvature. K_a is just the curvature of the generating curve, being positive when the wall is convex outwards and

negative when it is concave outwards. K_b is the reciprocal of the length of the normal intercepted between the curve and the axis of rotation.

Simulation of unsteady flow is possible, but in general the steady-state solution is obtained by solving equations numerically by advancing in time until the flow thickness in the whole flow domain does not vary with time. The momentum equations are used to calculate the velocity components u and w tangential to the back-wall, while the velocity component normal to the back-wall, v , is calculated from the continuity equation. All equations are approximated with the finite-difference formulas on a non-uniform grid that clusters more grid points near the back-wall and near the free surface where the flow and magnetic field gradients are expected to be high. If the mesh is uniform, the finite-difference scheme provides the second-order approximation with respect to both x and y . The two momentum equations are solved by the Blottner-type technique [11], which is well suited for marching problems. The induction equation is solved at each time step using the well-known ADI method.

The height function approach [12] is used for tracking the free surface. In this method, a new variable $y_l = y/h[x]$ is introduced. By instituting this change of variables, the curvilinear domain of integration is reduced to a rectangular shape that makes discretization of the equations and boundary conditions much easier, and along with the continuity equation provides mass conservation over the whole flow domain. The flow height, $h[x]$ is calculated simultaneously with other flow quantities using the kinematic free surface condition, which expresses the fact that the velocity vector at a steady free surface is tangential to the surface. This technique is an effective way of tracking free surface unless the surface is broken or demonstrates overturning waves (i.e. not a single-valued function). In these, more complex situations, more sophisticated free surface tracking algorithms should be used, such as VOF (volume of fluid method) or Level Set Method, which are also used in the present study and are explained below.

A similar numerical method for solving marching problems was used by the author in calculations of MHD turbulent open-channel flows. The method demonstrated high accuracy as well as good convergence in a wide range of flow parameters [13].

The numerical solution to Eqs. (6)–(9) is obtained for many cases, only a few of which are presented

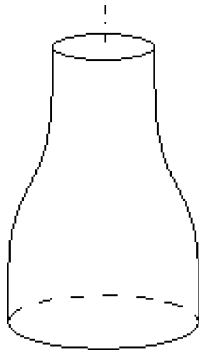
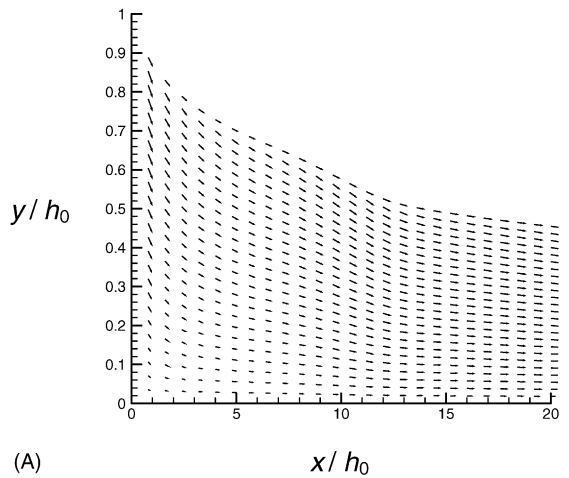


Fig. 2. The “bottle-neck” surface of revolution approximating the lower portion of a ST center-stack.

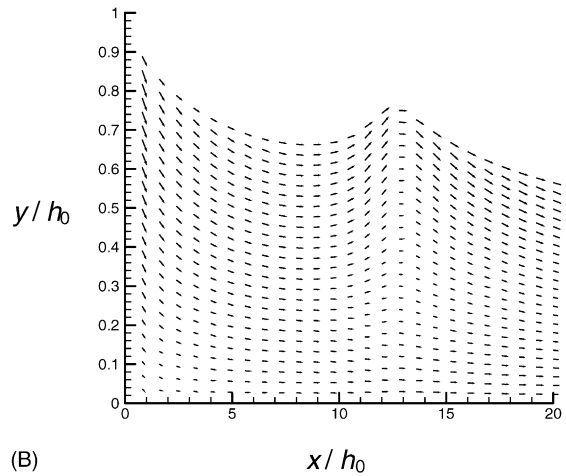
here. As a reference geometry we take a “bottle-neck” surface of revolution shown in Fig. 2 as a prototype for liquid-metal flow around the central column of the NSTX reactor near its basis. The liquid driven by a gravity force flows down over the surface forming a thin liquid layer. It is easy to see that all assumptions used in deriving the thin-shear-layer equations are met.

A basis for comparison, laminar flow without a magnetic field is shown in Fig. 3A. The flow thickness is monotonically reduced by the joint action of the gravity and the geometrical effect of flow area increase—that is the surface geometry causes a stretching (or contraction) of the streamlines of the main flow that results in a thinning (or thickening) of the layer.

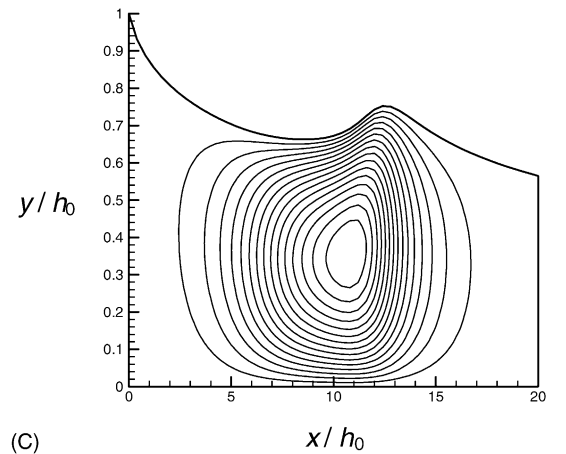
To illustrate the combined effect caused by the geometrical changes described above with the changes of the toroidal magnetic field, a $1/R$ toroidal field was considered. Under these conditions, only the currents in the x – y plane are induced, all electromagnetic forces are located in the same plane, so that no toroidal flow occurs. With the influence of the applied magnetic field the liquid is driven out of the flow bulk towards the free surface. This typically results in a “surface bump”. The bump occurs where the surface and hence the applied azimuthal magnetic field exhibit maximum changes. The magnetic field contour lines also represent the trajectories along which the electric current flows. One



(A)



(B)



(C)

Fig. 3. Simulations results for $Re = 23,500$, $Fr = 5.0$ open channel flow in a spanwise field with gradient. (A) Velocity vector plot in the x – y plane with no magnetic field, (B) velocity vector and (C) current streamline plot in the x – y plane with toroidal magnetic field $Re_m = 0.07$, $Ha_{max} = 8500$.

can see that the current takes its path within the flow domain and is stronger near the back-wall and free surface.

The MHD effects become even more interesting as one adds additional field components and observes the interaction of various components of field and induced current. If a wall normal field component is added to a constant toroidal magnetic field, then in the axisymmetric case, the two components do not interact. Motion in poloidal plane does not produce any current due to the constant toroidal field (except maybe near conducting nozzles), and the current created by the poloidal motion in the radial field produces only toroidal current. This toroidal current however will interact with the radial field to produce a strong drag effect. Since the assumption of axisymmetry provides a complete toroidal flow path for this toroidal current, no electric field can arise to oppose the current—meaning that the flow behaves like flow in a perfectly conducting channel. Some calculations done for APEX are given in Ref. [3] and show that fields larger than ~ 0.018 T for lithium and ~ 0.08 T for tin lead to unacceptable thickening of the flow. The conductivity of the back wall does not affect these results, unless one considers inserting toroidal dividers—breaking the axisymmetry.

When a small wall-normal component of the magnetic field additionally to the toroidal field with $1/R$ variation $\mathbf{B}^0 = (0, B_y^0, B_\theta^0[r])$ is considered, the result is a secondary toroidal flow. In the case under consideration, the secondary flow exists in the form of a swirl flow and is caused by the toroidal Lorentz force, which arises from the interaction between the currents in the

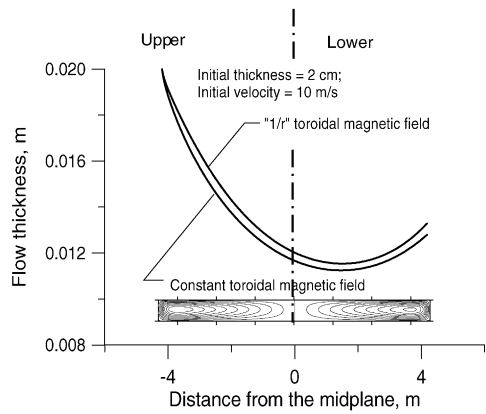


Fig. 5. Effect of toroidal field gradient on depth of lithium first-wall flow with $\mathbf{B}^0 = 10$ T.

x - y plane and wall-normal magnetic field. Fig. 4 illustrates the swirl flow effect. Although the wall-normal magnetic field is very small comparatively to the azimuthal field (only about 0.2% of the azimuthal field), the swirl flow is pronounced and even comparable with the main flow. The azimuthal Lorentz force is fully defined by the induced currents, which are oppositely directed near the back-wall and free surface (see the induced current distribution in Fig. 3C for example). Correspondingly, the liquid in the layer rotates in two opposite directions with strong shear over the thin layer.

Calculations have also been performed for a typical outboard liquid first-wall case in a reactor the scale of ARIES-RS where the flow will experience an average toroidal field gradient in the range of 0.25–1 T/m de-

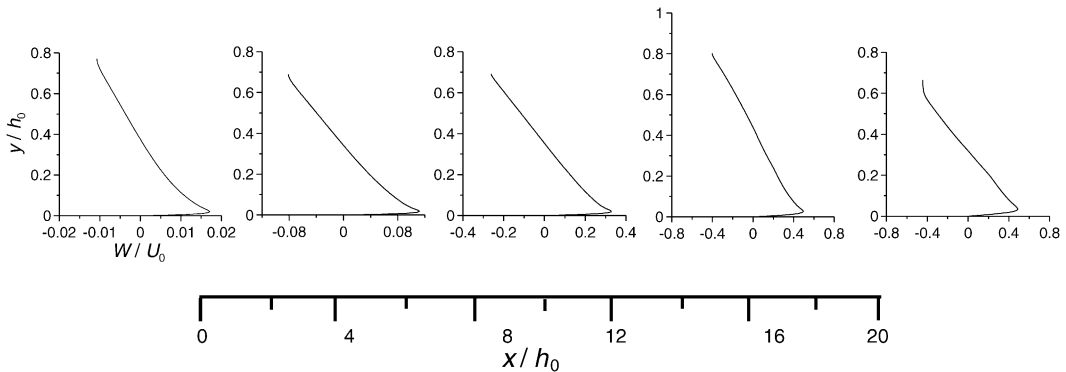


Fig. 4. Downstream variations of the toroidal velocity component (w) in a two component magnetic field. See geometry in Fig. 2 and parameters in Fig. 3.

pending on the first-wall geometry assumed. For a circular arc outboard flow geometry the lithium flow depth shown in Fig. 5 is affected only slightly by the field gradient drag effect. The relative drag effect (normalized by the liquid inertia) can be slightly stronger for conducting walls and much stronger for thicker or slower flows. When an alternate liquid like Sn is considered, the drag effect is much reduced due to the greater density (inertia) of Sn, and for these conditions no change in film height is observed due to the gradient effect.

The so-called magnetic propulsion current discussed earlier can be added to both of the above cases. Calculations [3] and recent experiments [14] have shown this current to be very effective in pushing the liquid against the back wall, aiding in liquid propulsion, and suppressing surface instabilities—potentially overcoming several of the problems discussed above for both first-wall and drain pipes. The most serious problem encountered with the magnetic propulsion idea is the effect of other field components on the flow dynamics. The use of streamwise magnetic propulsion currents in a case with wall normal field components will preferentially push the liquid in the toroidal/anti-toroidal direction depending on the sign of the radial field. For an axisymmetric flow, these types of toroidal motions may be acceptable. But if one considers toroidal breaks of any kind, liquid splashing and non-uniformity can result.

2.3. 2D modeling of instabilities in a non-uniform magnetic field

When a conducting liquid passes through a high magnetic field gradient zone, the liquid can redistribute to form velocity profiles with significant non-uniformity (such as the profiles shown in Fig. 1). These velocity distributions have inflection points and from the point of view of classic hydrodynamics can be unstable. Such flows in strong field gradients can be observed in fusion reactors when liquid metal is injected into the reactor chamber between toroidal field magnets, passing a zone of a high gradient magnetic field. Another example is a poloidal flow (such that in a blanket) in a strong toroidal reactor magnetic field, which varies as “ $1/R$ ”, where R is the distance from the chamber axis to a given point within the flow. In such flows, the field gradient can vary from 0.25 to 10 T/m or even higher, which is enough to trigger the instabil-

ity. From the point of view of hydrodynamic stability theory, these flows can be characterized in terms of the classic Raleigh–Tolmien point-of-inflection criterion, which links the instability to the shape of the basic velocity profile. A first order analytic analysis of the problem for free surfaces was given in Ref. [5], where the conclusion was reached that a more complete model that includes and accurate treatment of variations in the current as well as the velocity profiles was required.

Several models for Eqs. (1)–(3a) and (5) that assume only a toroidal field component without curvature effects have been developed and applied to the flow stability problem. Both flows in closed channels and with free surfaces are considered.

2.3.1. Instabilities in closed channel flows

In the present phase of APEX, flow instabilities in closed channels were studied for a case of a spatially varying magnetic field [15]. The computer code solves 2D Navier–Stokes–Maxwell equations that use vorticity, stream function and induced magnetic field as basic variables using a time-marching procedure that extends the standard ψ – ω approach described in [16] for non-MHD flows. The governing equations were approximated explicitly with finite-difference formulas on a uniform mesh. The discretization is of first-order in time and second-order in space. Advancing in time is performed in the following way:

$$\frac{\tilde{\omega}^{n+1} - \tilde{\omega}^n}{\Delta \tilde{t}} = \hat{L}_\omega \tilde{\omega}^{n+1} + \hat{F}_\omega^n, \quad (10a)$$

$$\frac{(\tilde{B}_z^i)^{n+1} - (\tilde{B}_z^i)^n}{\Delta \tilde{t}} = \hat{L}_B (\tilde{B}_z^i)^{n+1} + \hat{F}_B^n, \quad (10b)$$

$$\frac{\tilde{\psi}^{n+1,k+1} - \tilde{\psi}^{n+1,k}}{\Delta \tilde{\tau}} = \hat{L}_\psi \tilde{\psi}^{n+1,k+1} + \hat{F}_\psi^n. \quad (10c)$$

Here, \hat{L} is a 2D finite-difference operator that approximates the diffusive and convective terms by second-order formulas. \hat{F} the finite-difference approximation of the source term, which also has second-order accuracy. Central-difference approximations were used for the discretization of the diffusive terms. In the vorticity transport equation, the second-order monotonic Samarskii scheme [17] was employed as an approximation of the convective terms. This scheme possesses smaller schematic viscosity in comparison with the up-

wind schemes and is widely used in computations of convective flows for which adequate representation of the non-linear terms is especially important. The finite-difference equation for the stream function was formulated in a pseudo-transient form by introducing a pseudo-time term and solved by iterations at each time step. Upon convergence, the pseudo-time term vanishes, and the original Poisson equation is satisfied. The expressions for the electric current components and those for the velocity components were also approximated with the second-order formulas.

A particular example of a fringing magnetic field was considered when an electrically conducting fluid enters a gap between the magnet poles. An applied magnetic field was simulated with the following expression: $B_z^0 = B_0 / (1 + \exp[-\alpha(x - x_0)])$. By varying B_0 and α , flow regimes were sought in which an initially non-disturbed flow transitions to an unstable one. Quasi-periodic flow regimes were observed similar to those in ordinary hydrodynamic flows around a cylinder. Downstream of the magnetic field gradient zone, a wake formation occurs resembling the Karman vortex street behind a bluff body. However details of the flow patterns observed in the present MHD case were different because of the magnetic field effects. The two shear layers formed in the wall vicinity when

the liquid passes the field gradient zone, under some critical values of the flow parameters become unstable. Corresponding instability patterns for the flow stream function and vorticity are shown in Fig. 6.

The instability appears if the velocity demonstrates inflection points (similar to the analytic stability solution [5]). If the inflection points are not very pronounced, the instability does not appear because the instability mechanism associated with the inflection points is not strong enough against the stabilizing effect due to the Joule and viscous dissipation. Also, the instability does not appear if Re is small, even though Ha_∇ is high, since viscous forces damp perturbations. However, full conclusions on stability/instability can be drawn only on the basis of a more detailed stability analysis.

2.3.2. Instabilities in free surface flows

Distinct from the codes described in Section 2.2, a series of free surface codes that utilize the *volume of fluid* (VOF) technique have also been developed. VOF follows the advection of a fluid f with unit “density” and reconstructs the interface based on the ∇f information (e.g. see Puckett et al. [18]). It allows for large deformation of the free surface to occur without loss of robustness. The dynamic conditions at free sur-

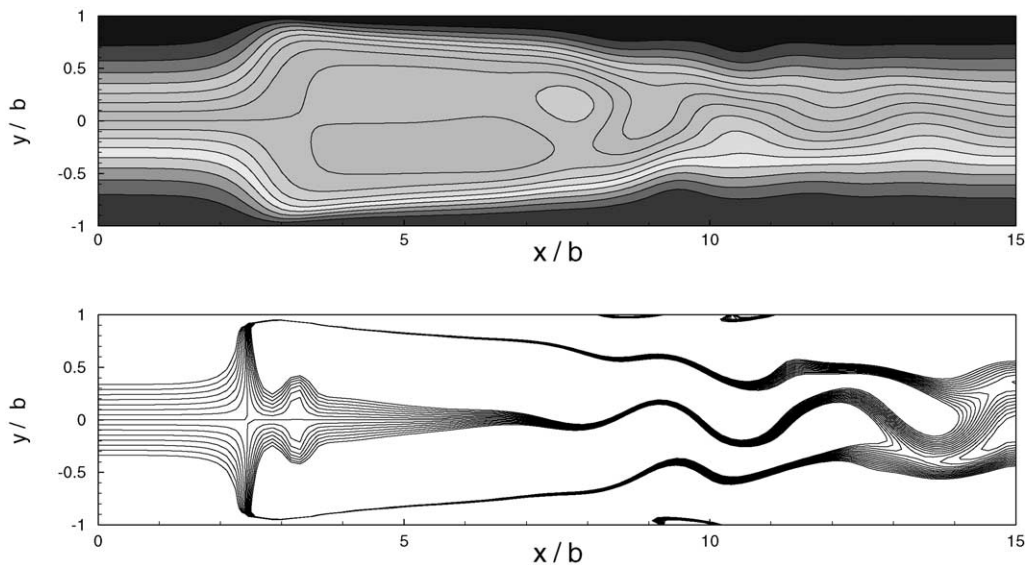


Fig. 6. Unsteady stream function and vorticity behavior in MHD flow in a fringing magnetic field with $Re = 200$ and $Ha_{\max} = 200$. The instability develops downstream of the magnetic field gradient zone. The observed structures resemble the Karman vortex street behind a bluff body.

face are implemented via the continuum surface force (CSF) model [19]. The Navier–Stokes equations are solved in a two-step projection method, and the induction equation is solved implicitly for the induced field. The numerical scheme has been validated in regard to the Navier–Stokes solver by simulating thin water film flows and magnetic mechanism implementation by computing MHD films and comparing with analytical solution and other numerical results. The model is described in detail in several of the Refs. [20,21].

When the liquid is flowing downstream, the liquid–gas interface $h[x, t]$ changes with the streamwise location and time, which is defined by the kinematic equation:

$$v[x, y = h] = \frac{\partial h}{\partial t} + u[x, y = h] \frac{\partial h}{\partial x}. \quad (11)$$

At the free surface the normal stress is balanced by the capillary force, and the shear stress vanishes for the constant surface tension condition.

As seen in the electric current distributions shown earlier in Figs. 3 and 5, there is a concern that arises from the fact that the streamwise currents flow in one direction near the surface and in the opposite direction near the back wall. This current pattern results in a force near the surface that tries to pull the liquid into the plasma. This force integrates to zero over the entire depth of the liquid film if the back wall is electrically insulated, but may have implications on the surface stability of the flow. If the back wall is conducting, there will be a net force pulling or pushing the liquid relative to the wall and issues of flow detachment arise.

A case is explored here that approximates flow on an inverted upper half of an outboard first-wall in the ARIES-RS reactor, assumed to be the most unstable part of the flow path. The flow is inverted to gravity and initiated with 10 m/s slug flow into a 1 m long computational area. A magnetic field is considered such that:

$$B_z^0 = \begin{cases} 11T, & x < 0.05, \\ \frac{11 \times (5.5)}{(x - 0.05 + 5.5)} T & x > 0.05, \end{cases} \quad (12)$$

where an initially constant magnetic field begins to vary 5 cm downstream from the computational inlet. The flow is perturbed by relaxation of the velocity profile.

Looking at a lithium flow shown in Fig. 7 over the 1 m length we see the growth of a fairly strong instabil-

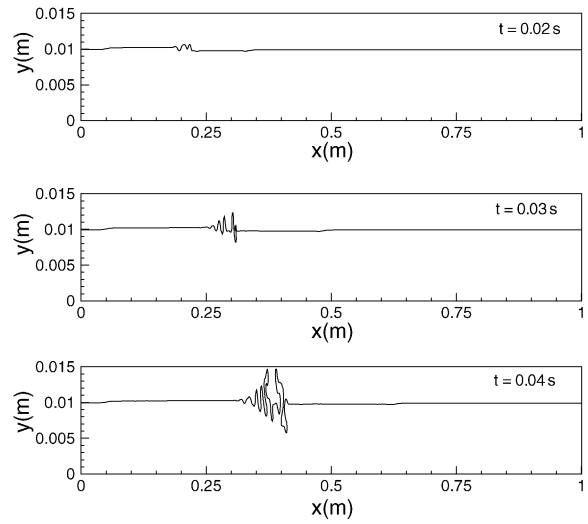


Fig. 7. Instability growth on a 1 cm deep, 10 m/s flow of lithium into a typical 1/R toroidal field gradient beginning at $x = 0.05$ m.

ity from the initial small bump. An identical calculation using tin properties shows no visible growth of instability over the same period of time. (Instability is seen in cases analyzed with lower inlet velocity where the inertia of the tin is not so high.) The effects of stronger field gradients on thicker flows was investigated in Ref. [4] where considerably more dramatic effect was observed, even for tin, owing to the large field gradient and thicker layer. The strength of the magnetic interaction is particularly sensitive to the flow depth, one reason that thin layers for liquid first-wall and divertor applications have been pursued in APEX rather than neutronically thick liquid wall concepts.

In all cases, the application of magnetic propulsion current [9] was useful in stabilizing the surface shape and propelling the liquid through the gradient region. For the conditions in Fig. 7, the flow behaves as shown in Fig. 8 with 100 A/m applied current in the main flow direction. It should be noted that the magnetic propulsion concept is suitable for flows from strong to weak field (inboard to outboard) or smaller area to larger area (again, inboard to outboard). It cannot be applied universally for any MHD flows.

This area of research needs considerably more investigation to outline the conditions under which serious instabilities are expected in free surface flows, especially as more complex geometries and fields are considered that require a full 3D treatment.

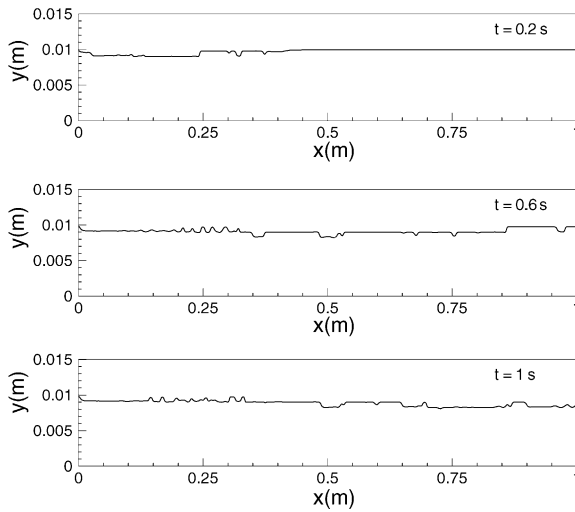


Fig. 8. Instability growth on a 1 cm deep, 10 m/s flow of lithium into a typical $1/R$ toroidal field gradient beginning at $x = 0.05$ m with 100 A/m of streamwise current applied.

3. Fully 3D LM-MHD models and results

It was recognized by the conclusion of the first phase in APEX that a numerical tool that can handle complex 3D geometry free surface MHD flows would be an extremely valuable aid to the understanding of liquid wall flows. It was also recognized that it would take considerable effort to develop such a capability, and even if successful, the code might be very limited in the range of Hartmann number if steps were not taken in the beginning to overcome as much as possible inherent limitations in formulation or numerical methodology. Initially, effort was put into writing an MHD module to work with the FLOW3D commercial software package (in use at UCLA to investigate 3D free surface flows without MHD). The module met with limited success, the main problem being extremely long computational times for large jobs and no access to the source code for necessary modifications [22,23].

So the design of a new numerical tool specifically formulated to overcome the limitation of existing tools was initiated. The work on the HIMAG (HyPerComp Incompressible MHD solver for Arbitrary Geometries) code is presented here in some detail, as it is the first time any of code formulation and results have been published. Still, a more complete reference to the code structure and formulation is available in [24].

3.1. HIMAG 3D free surface MHD code

At the beginning of the code design the following choices were made which guided the formulation of the code:

1. Unstructured grid formulation to allow any geometry of fluid flow, nozzles, obstructions, etc. to be accommodated, and allow high resolution of thin Hartmann type boundary layers at high Hartmann number with a minimum of cells.
2. Parallel solver implementation to allow large problem sizes and “stiff” matrices to be solved in an acceptable amount of wall clock time.
3. Flexible implicit framework for using various free surface tracking (level-set, VOF, etc.) and electric current (potential formulation, induced-B formulation, etc.) modules and for reducing time-step restrictions.

HIMAG has been developed as an extension to the HyPerComp electromagnetics code environment [25], and compressible MHD code development activities [26]. HIMAG has inherited a parallel, unstructured code environment from the electromagnetics software, and has essentially replaced the solver and code integration strategies. In its present form, the following capabilities are available in HIMAG:

- 3D incompressible flow solver (second-order accurate in space and time);
- free surface capture using level set technique;
- arbitrary mesh structure (unstructured/hybrid);
- parallel code environment using MPI;
- computation of electromagnetic fields using the electric potential formulation;
- point implicit scheme, solved in an iterative manner;
- multiple strategies to account for mesh skewness (non-orthogonality);
- modular addition of source terms;
- graphical user interfaces.

Besides the development of the solver, a significant effort was expended in studying alternate MHD models (based on induced magnetic field and induced current,) to overcome certain limitations of the electric potential approach. These limitations tend to be chiefly numerical and become progressively more prominent at higher Hartmann numbers and magnetic field intensities [27].

3.1.1. Model formulation

In this section, we describe the governing equation sets for the flow phenomena that we intend to simulate and study. Each individual phenomenon is modeled separately and their mutual interactions are “loosely” coupled, in the terminology of multi-physics.

3.1.1.1. Conservation of mass and momentum—primitive variable formulation. Incompressible flow is governed by the continuity and momentum equations given below, frequently referred to as the incompressible Navier–Stokes equations.

$$\frac{\partial \mathbf{v}}{\partial t} + (\mathbf{v} \cdot \nabla) \mathbf{v} = -\frac{1}{\rho} \nabla p + \underbrace{\nabla \cdot \boldsymbol{\tau}}_{\text{viscous}} + \mathbf{g} + \underbrace{\frac{1}{\rho} \mathbf{j} \times \mathbf{B}^0}_{\text{MHD}} + \underbrace{\mathbf{F}_s}_{\text{surface tension}} \quad (13a)$$

$$\nabla \cdot \mathbf{v} = 0. \quad (13b)$$

The momentum equation above has contributions due to viscous, MHD, gravitational and surface tension forces, all of which may be present in free surface MHD. The basic fluid quantities that are to be determined from this set, are the velocity components u, v, w (in the x, y, z directions respectively,) and the pressure p . While the momentum equation provides a time advancement of the velocity components, pressure must be derived using some external procedure that will guarantee the conservation of mass (continuity). In HIMAG, we use the projection method, wherein a pressure field is derived from an updated momentum field such that the divergence of velocity at the new time level is zero.

3.1.1.2. Free surface capture—level set technique. We have elected to use the level set technique [28] to model the advancement of free surfaces present in the flow. A function φ is defined such that its value is zero on the interface separating the two fluids: a lighter fluid-2 and a heavier fluid-1, as shown in Fig. 9. Away from the interface, the value of φ is given as the normal distance from the interface, negative into fluid-2 and positive into fluid-1. This function is advanced in time in a Lagrangian fashion on the fluid mesh using the local fluid velocity, and is related to the fluid properties such as density and viscosity through the Heaviside

function $H[\varphi]$:

$$\frac{\partial \varphi}{\partial t} + \mathbf{v} \cdot \nabla \varphi = 0, \quad (14a)$$

$$\rho = \rho_1 + (\rho_2 - \rho_1)H[\varphi], \quad (14b)$$

$$\mu = \mu_1 + (\mu_2 - \mu_1)H[\varphi]. \quad (14c)$$

Though the interface is ideally of zero thickness, this is unattainable in practical numerical simulations using this technique, and non-physical oscillations in the computed solutions can occur. The Heaviside function is therefore smeared about the zero level by an amount ε that may depend on the local mesh resolution. Fig. 9 illustrates this effect.

3.1.1.3. Electromagnetics—electric potential formulation. If $Re_m \ll 1$, the induced magnetic field may be neglected in the calculation of the body force terms $\mathbf{j} \times \mathbf{B}^0$. In such a situation, the electric field may be derived from a scalar potential:

$$\mathbf{E} = -\nabla \phi \quad (15)$$

and current may be computed using Ohm’s law:

$$\mathbf{j} = \sigma(-\nabla \phi + \mathbf{v} \times \mathbf{B}^0). \quad (16)$$

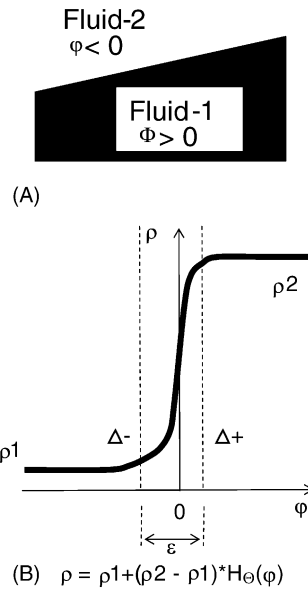


Fig. 9. (A) Graphical representation of the level set function φ , and (B) smeared Heaviside function.

The only electromagnetic field quantity that needs to be computed numerically at each time step is the electric potential. This potential is governed by the following elliptic differential equation that is obtained by enforcing conservation of current through setting the divergence of the current density equation (16) to zero:

$$\nabla^2 \phi = \nabla \cdot (\mathbf{v} \times \mathbf{B}^0) + \nabla(\log \sigma) \cdot (-\nabla \phi + \mathbf{v} \times \mathbf{B}^0). \quad (17)$$

In a single fluid medium, electrical conductivity is constant, and the second term on the right hand side above vanishes. At interfaces (solid as well as liquid,) where the electrical conductivity has a gradient, this equation must be written in a weak form, since the gradient of the conductivity is infinite. At an interface across which the conductivity becomes zero, the component normal to the interface, the normal component of current is explicitly forced to be zero (in a fully conservative form, this can cause division by zero):

$$\nabla_n \phi = \mathbf{v} \times \mathbf{B}^0|_n. \quad (18)$$

There are of course many other EM formulations, like the induced-B used in the 2D axisymmetric codes described in the Section 2 of this paper, variants on the vector potential formulation, or even direct \mathbf{j} formulations [27,29]. While some of these are considered for future development in HIMAG, the electric potential approach has been adopted here as the first stage, and investigating the extent to which this formulation can be applied for high Hartmann number is one of the many research subjects we wish to address.

In order to allow the modeling of liquids with non-isotropic electrical conductivity, namely plasmas that have greater conductivity along magnetic field lines than perpendicular to them, we have re-derived the electric potential equation to allow such anisotropy:

$$\begin{aligned} & \nabla \cdot (\sigma_{\perp} \nabla \phi + (\sigma_{\parallel} - \sigma_{\perp})(\nabla \phi \cdot \mathbf{b})\mathbf{b}) \\ & = \nabla \cdot (\sigma_{\perp} \mathbf{v} \times \mathbf{B} + (\sigma_{\parallel} - \sigma_{\perp})((\mathbf{v} \times \mathbf{B}^0) \cdot \mathbf{b})\mathbf{b}). \end{aligned} \quad (19)$$

In the above, we use the symbol $\mathbf{b} = \mathbf{B}^0/|\mathbf{B}^0| = (b_x, b_y, b_z)$ to represent a unit vector in the direction of \mathbf{B}^0 . The quantities σ_{\perp} and σ_{\parallel} represent the conductivity in the directions normal to and parallel to the applied magnetic field \mathbf{B}^0 . A more general form of the conductivity tensor may be implemented with relative ease. However, since a comprehensive plasma model is not

the primary intent in this research at present, this has been deferred to a later time.

3.1.1.4. Heat conduction. HIMAG presently utilizes of a simple heat transfer model wherein convective and diffusive effects are modeled for essentially isotropic fluids and solid walls. The following form of the heat equation is solved:

$$\frac{\partial T}{\partial t} + \mathbf{v} \cdot \nabla T = \nabla \cdot \alpha \nabla T \quad (20)$$

The thermal diffusivity α depends on the level set function in a similar manner to density and the coefficient of viscosity.

3.1.1.5. Solid walls and obstacles. It is possible to define solid walls in HIMAG by flagging the material cells during generation the computational mesh. This flag is imported in the solver and different material properties are assigned to the cells in solid regions. Multiple solid materials are possible and a database of solid properties is maintained. The finite volume formulation used in HIMAG enables an easy treatment of face fluxes at internal solid boundaries. Velocity and the normal pressure gradient are set to zero at an internal solid boundary.

3.1.2. Numerical technique

In this section, the numerical formulation for second-order accuracy in space and time on unstructured meshes is presented. To preserve a second-order spatial accuracy, it is often necessary on non-uniform meshes to interpolate quantities from neighboring cell centers to a cell face using a fast and accurate interpolation procedure. When a quantity φ is extrapolated to the cell face from a cell center using the locally averaged value of the gradient within the cell, the accuracy is formally second order. However, in order to enforce conservation, it may be necessary to average between this value and the corresponding value obtained from the neighboring cell. These operations tend to be expensive, and we have found a simple distance based interpolation to work well for even highly stretched meshes.

First the perpendicular distance is computed from a current cell P and a neighboring cell N to their common face whose centroid is denoted by G. If the mesh is orthogonal, the following interpolation law may be used for φ_f , the value of φ at the cell face (the vector \mathbf{a}

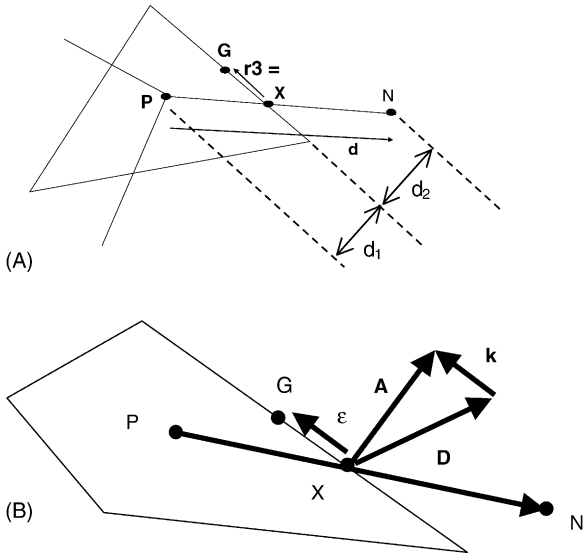


Fig. 10. Important vectors and distances in interpolating quantities to cell faces, (A) face normal distances, (B) projection of orthogonal and non-orthogonal contributions.

is the face normal area vector):

$$d_1 = \left| \frac{a_x(x_P - x_G) + a_y(y_P - y_G) + a_z(z_P - z_G)}{\sqrt{a_x^2 + a_y^2 + a_z^2}} \right|, \quad (21a)$$

$$d_2 = \left| \frac{a_x(x_N - x_G) + a_y(y_N - y_G) + a_z(z_N - z_G)}{\sqrt{a_x^2 + a_y^2 + a_z^2}} \right|, \quad (21b)$$

$$\varphi_f = \frac{d_2\varphi_P + d_1\varphi_N}{d_1 + d_2}, \quad \text{or} \quad \varphi_f = f\varphi_P + (1 - f)\varphi_N, \quad (21c)$$

where $f = \frac{d_2}{d_1 + d_2}$.

If the mesh is non-orthogonal, or skewed, a further correction may be made to relocate this quantity to the cell center. Fig. 10 shows a stencil where the quantity φ needs to be relocated from f to G , the centroid. A gradient is evaluated from Gauss' rule, using the thus far interpolated value φ_f , and averaged between neighboring cells, to get a cell face value.

$$\nabla\varphi|_P = \sum_{\text{faces}} \varphi_G \frac{\vec{a}}{a}, \quad (22a)$$

$$\varphi_G = \frac{d_2\varphi_P + d_1\varphi_N}{d_1 + d_2} + \frac{1}{2}[\nabla\varphi|_P + \nabla\varphi|_N]r_3 \quad (22b)$$

This, in effect, changes the face value φ_f that was used in computing the gradient in the Gauss integral formula. This procedure is iterated for convergence. Typically, 3–4 iterations were sufficient to recover the exact value of the gradient of a linear field on a highly skewed triangular mesh.

3.1.2.1. A fractional step method for interfacial flow. The momentum equation can be written using the Crank–Nicholson (trapezoidal) time differencing of the non-linear advective and the linear diffusive terms, to yield:

$$\begin{aligned} & \frac{(u_i)^{n+1} - (u_i)^n}{\Delta t} + \frac{1}{2} \frac{\partial}{\partial x_j} (u_i^{n+1} u_j^{n+1} + u_i^n u_j^n) \\ &= -\frac{1}{\rho} \frac{\partial p^{n+1}}{\partial x_i} + \frac{1}{2\rho} \frac{\partial}{\partial x_j} \left(\mu \frac{\partial}{\partial x_j} (u_i^{n+1} + u_i^n) \right) \\ &+ F_{\text{MHD}}^n + F_s^n. \end{aligned} \quad (23)$$

Linearizing about time level n , and making no assumptions about the magnitude of change in momentum ρu (we do not show the body force terms in Eq. (24) for simplicity of presentation):

$$\begin{aligned} & \frac{(u_i)^{n+1} - (u_i)^n}{\Delta t} + \frac{1}{2} \frac{\partial}{\partial x_j} (u_i^{n+1} u_j^n + u_i^n u_j^{n+1}) \\ &= -\frac{1}{\rho} \frac{\partial p^{n+1}}{\partial x_i} + \frac{1}{2\rho} \frac{\partial}{\partial x_j} \left(\mu \frac{\partial}{\partial x_j} (u_i^{n+1} + u_i^n) \right), \end{aligned} \quad (24a)$$

$$\frac{\partial u_i^{n+1}}{\partial x_i} = 0. \quad (24b)$$

The fractional step method attempts to construct a velocity field at time level $n + 1$ from successive operations upon the field at time level n . First, an intermediate field bearing a superscript $*$ is computed, by removing the pressure gradient term. Then, a pressure field at time level $n + 1$ is computed in such a way as to project the velocity u^* into the space of discretely incompressible functions from which a velocity field u^{n+1} is then obtained. (The initial pressure field is calculated by solving the pressure equation utilizing the initial velocity conditions.) This procedure is some times referred to

as a projection method. We follow the schemes outlined by [30–32], following suggestions of [33] and [34] for variable density, and [35] for implementation the projection method scheme on a co-located (i.e. non-staggered) mesh:

$$\begin{aligned} \frac{(\hat{u}_i) - (u_i)^n}{\Delta t} + \frac{1}{2} \frac{\partial}{\partial x_j} (\hat{u}_i u_j^n + u_i^n \hat{u}_j) \\ = -\frac{1}{\rho^n} \frac{\partial p^n}{\partial x_i} + \frac{1}{2\rho^n} \frac{\partial}{\partial x_j} \left(\hat{\mu} \frac{\partial}{\partial x_j} (\hat{u}_i + u_i^n) \right), \end{aligned} \quad (25a)$$

$$\frac{(u_i^*) - (\hat{u}_i)}{\Delta t} = \frac{1}{\rho^n} \frac{\partial p^n}{\partial x_i}, \quad (25b)$$

$$\frac{\partial}{\partial x_i} \left(\frac{1}{\rho^{n+1}} \frac{\partial p^{n+1}}{\partial x_i} \right) = \frac{1}{\Delta t} \frac{\partial u_i^*}{\partial x_i}, \quad (25c)$$

$$\frac{(u_i^{n+1}) - (u_i^*)}{\Delta t} = -\frac{1}{\rho^{n+1}} \frac{\partial p^{n+1}}{\partial x_i}. \quad (25d)$$

Density is advanced in time by solving the level set equation, as will be described below. While a full matrix inversion solution strategy for the entire domain is possible and is commonly used in structured meshes, an over-relaxation based iterative solution is used in our work. In practice, it has been seen that the equation set as presented above converges within 4–5 iterations to within about 10 orders of magnitude. A cell centered as well as a face based iteration strategy have both been used with almost equal performance.

3.1.2.2. Discretization of the level set equations. In the level set method, the level set function φ is first advanced using a simple discrete Lagrangian advection law:

$$\frac{\partial \varphi}{\partial t} + u_i \frac{\partial \varphi}{\partial x_i} = 0. \quad (26)$$

Then, it is re-initialized such that its distribution is smooth, and that it retains its “distance function” property, whereby the value of φ at any given point is the closest distance to the liquid–gas interface:

$$\frac{\partial \varphi}{\partial \tau} + \left(\text{sign}(\varphi_0) \frac{\nabla \varphi}{|\nabla \varphi|} \right) \cdot \nabla \varphi = \text{sign}(\varphi_0). \quad (27)$$

A total variation diminishing (TVD) scheme is used advance the level set function at each time step. In this approach, we essentially limit the gradient of φ inside

a given cell, such that local spikes, or dips in this quantity are smoothed [37]. However, this approach is not directly applicable to the level set reinitialization equation (27) where a second-order upwind version of the shape-from-shading approach of Ruoy and Tourin [36] is used, extended here to unstructured mesh systems. Higher order corrections, and source terms to account for mass loss errors from the level set method, have been incorporated. Details of this implementation will be presented in a future publication. It must be borne in mind that the Heaviside function, relating density to the level set function, is typically smoothed over a region that is up to 2–3 computational cells wide. It can be made sharper near convergence, or steady state. However, if the flow is dominated by transient processes, a smoother Heaviside function has been seen to be helpful.

3.1.2.3. Continuum surface force model of surface tension. The evaluation of the surface tension force is greatly facilitated in the level set formalism since the curvature of the free surface may be computed from derivatives of the continuous function φ . The continuum surface force (CSF) model [19] is used in HIMAG, where the surface tension force is added as a spatially varying body force to the Navier–Stokes equations, while it is sizeable only near the free surface. The expression for the surface tension force is:

$$F_s = \sigma_t \bar{\kappa} \nabla \varphi \delta(\varphi), \quad \text{where } \bar{\kappa} = \nabla \cdot \left(\frac{\nabla \varphi}{|\nabla \varphi|} \right) \quad (28)$$

and the delta function (smoothed over a distance ε), is given as:

$$\delta_\varepsilon(\varphi) = \begin{cases} \frac{1}{2\varepsilon} \left(1 + \cos \left(\frac{\pi \varphi}{\varepsilon} \right) \right) & \text{if } |\varphi| < \varepsilon, \\ 0 & \text{otherwise} \end{cases} \quad (29)$$

3.1.2.4. Computation of physical properties. The level set function is related to the density, viscosity, thermal and electrical conductivities via a smoothed Heaviside function, as follows:

$$\rho = \rho_1 + (\rho_2 - \rho_1) H_\varepsilon(\varphi) \quad (30a)$$

$$\mu = \mu_1 + (\mu_2 - \mu_1) H_\varepsilon(\varphi), \quad (30b)$$

$$\sigma = \sigma_1 + (\sigma_2 - \sigma_1) H_\varepsilon(\varphi), \quad (30c)$$

where the Heaviside function is defined numerically as:

$$H_\varepsilon(\varphi) = \begin{cases} 0 & \text{if } x < -\varepsilon, \\ \frac{x + \varepsilon}{2\varepsilon} \frac{\sin(\pi x/\varepsilon)}{2\pi} & \text{if } |x| \leq \varepsilon, \\ 1 & \text{if } x > \varepsilon. \end{cases} \quad (31)$$

3.1.2.5. Pressure Poisson equation on an arbitrary mesh. The pressure Poisson equation is solved in two distinct ways, based on the orthogonality of the mesh. Numerical representation of the pressure gradient normal to the cell face separates the two situations:

$$\begin{aligned} \nabla \cdot \frac{\nabla p}{\rho} &= \frac{\nabla \cdot \bar{\nabla}^*}{\Delta t} \Rightarrow \frac{1}{\Omega} \sum_{\text{faces}} \frac{1}{\rho} \frac{\partial p}{\partial n} \Delta s \\ &= \frac{1}{\Omega \Delta t} \left(\sum_{\neq BC} U^* \Delta s + \sum_{=BC} U^{n+1} \Delta s \right) \end{aligned} \quad (32)$$

where the summations on the right hand side are different for boundary faces and internal faces, and Δs denotes the cell face area and Ω the cell volume.

For an orthogonal mesh (face normal has the same direction as the line joining cell centers) a straightforward face-centered differencing expression should be second-order accurate. The following expressions are used:

$$\frac{\partial p}{\partial n} = \left(\frac{p_N - p_P}{d} \right) \frac{\mathbf{d}}{d} \cdot \hat{\mathbf{n}}, \quad (33a)$$

$$\frac{\partial p}{\partial n} = \left(\frac{p_N - p_P}{\mathbf{d} \cdot \hat{\mathbf{n}}} \right), \quad (33b)$$

where $\hat{\mathbf{n}}$ denotes a unit normal to the cell face. For a non-orthogonal (skewed) mesh an ‘‘over-relaxed’’ approach presented [38] has been used:

$$\frac{\partial p}{\partial n} = \frac{1}{\Delta s} \left(|\mathbf{D}| \frac{p_N - p_P}{|\mathbf{d}|} + \mathbf{k} \cdot (\nabla p)_f \right), \quad (34)$$

where the gradient of p is evaluated at the face centroid using an interpolation formula.

A linear interpolation $(\nabla p)_f = \alpha(\nabla p)_P + (1 - \alpha)(\nabla p)_N$ where the constant α is a value between zero

and unity, essentially works by increasing the stencil used in the non-orthogonal contribution. The gradient of p itself, is evaluated by a simple Gauss summation:

$$\nabla p = \frac{1}{\Omega} \sum_{\text{faces}} p_f \Delta \mathbf{s}, \quad (35)$$

where p_f represents the value of pressure interpolated to the cell face. A matter of some concern is the re-location of this quantity from the intersection of line joining the cell centers with the cell face (labeled X in Fig. 10), to the centroid of the cell face (G). This may be done by iteratively using the gradient of pressure data that is available from its last estimate, and correcting it thus:

$$p_f|_G = p_f|_X + (\nabla p)_f^* \cdot \boldsymbol{\varepsilon} \quad (36)$$

where the ∇p^* at the cell face is its last evaluated value, linearly interpolated to the cell face, and the vector $\boldsymbol{\varepsilon}$ is the vector joining the intersection point to the face centroid. In general, an over-relaxation factor is used in pressure computation, as follows:

$$p^{n+1} = p^n + \omega(p^* - p^n) \quad (37)$$

where p^* is the newly computed quantity and ω the relaxation factor, typically, 1.7–1.9. The choice of this relaxation factor is restricted when used in the parallel mode. A conservative choice of $\omega = 1.0$ is used in parallel runs.

3.1.2.6. Electric potential equation. Eq. (19) is converted into its conservative finite volume equivalent, and solved using the point relaxation technique. In the finite volume method, the divergence operators are converted into volume integrals and there upon, into surface integrals using Gauss’ law as follows:

$$\nabla \cdot \mathbf{F} = \int_{\Omega} \mathbf{F} \mathbf{d}\Omega = \int_{\partial\Omega} \mathbf{F} \mathbf{d}\mathbf{s} \quad (38)$$

Using the standard notation of finite volume method, and the notation introduced in the pressure Poisson solution description, we can obtain the final discrete version of the current conservation law (Eq. (19)) in terms of the electric potential, as:

$$\phi_P = \frac{\sum_{\text{faces}} ((\sigma_{\perp}/\mathbf{d}) + ((\sigma_{\perp} - \sigma_{\parallel})(\mathbf{b} \cdot \mathbf{d})(\mathbf{b} \cdot \mathbf{n})/d^2)) \phi_N \Delta s + \sum_{\text{faces}} (\sigma_{\perp}(\mathbf{v} \times \mathbf{B}^0) + ((\sigma_{\perp} - \sigma_{\parallel})(\mathbf{v} \times \mathbf{B}^0) \cdot \mathbf{b}) \mathbf{b}) \cdot \Delta \mathbf{s}}{\sum_{\text{faces}} ((\sigma_{\perp}/\mathbf{d}) + ((\sigma_{\perp} - \sigma_{\parallel})(\mathbf{b} \cdot \mathbf{d})(\mathbf{b} \cdot \mathbf{n})/d^2)) \Delta s} \quad (39)$$

with the appropriate non-orthogonal corrections where desired. In general, we solve this equation using point-wise over-relaxation, with a relaxation factor 1.7–1.9.

3.1.3. Initial and boundary conditions

In HIMAG, the boundaries of the computational domain are divided into “patches”, and boundary conditions are prescribed on each patch for each of the variables: u , v , w , p , ϕ , ψ , and T . At inflow boundaries, the velocity may be prescribed and pressure extrapolated from within the domain. At an outflow boundary, velocity may be extrapolated and a pressure (if known) specified. A pure Neumann boundary condition for pressure and electric potential is available. Here, only the gradient of these quantities normal to the boundary are known. For instance, for the electric potential, a current tangency condition at an insulating wall requires that $\nabla_n \phi = (\mathbf{v} \times \mathbf{B}^0)_n$ in order to make the wall normal current zero. A Neumann condition for pressure is used when the pressure distribution across a surface is expected to be non-uniform or simply unknown. Whenever a Neumann BC is used, care must be taken to fix the value of p or ϕ at one interior cell. In HIMAG, cell number 1 is chosen for this purpose. In a parallel computation, the cell number 1 on the host node is used as the reference cell. The quantity p is set to zero in this cell in each iterative cycle, and its computed value is subtracted from all the cells.

Five different BC-types are presently available in HIMAG. They are: velocity, level set, pressure, electromagnetic, and thermal BCs. Table 2 shows a full list of BCs that are currently available from HIMAG-PREP, the graphical interface to HIMAG.

3.1.4. Solution acceleration

There are several solution acceleration devices present in the code at this time. HIMAG presently uses the Crank–Nicholson implicit schemes for the non-linear advective terms as well as the viscous terms in the momentum equations to allow the possibility of large (or variable) time steps. This scheme is applied in a point implicit sense. That is to say that the entire system of equations containing the unknown variables at the $n + 1$ level is not inverted at once. This is due to the fact that the code is capable of handling arbitrary geometries, and the coefficient matrices tend to be dense and expensive to invert. Also, since the boundary condi-

Table 2
HIMAG boundary condition types

	Unique ID
Velocity BCs	
Inflow	
Velocity profile from file (enter value)	1
Constant velocity (enter value)	2
Outflow	
Characteristic BC for V	3
Neumann BC for V	4
No Slip (viscous) wall	5
Slip (inviscid) wall	6
Far field (free stream)	
Characteristic BC	7
Neumann BC	8
Fixed BC (enter value)	9
Pressure BCs	
Constant value (specify)	1
Neumann	2
Level Set BCs	
Fixed polynomial for level set function (specify coefficients in x , y , z -linear: $\phi = ax + by + cz + d$)	1
Neumann	2
Specified contact angle	3
Thermal BCs	
Fixed temperature (specify value)	1
Adiabatic	2
Electromagnetic BCs	
Specified potential	1
Neumann (current free)	2
Thin conducting wall (specify thickness, sigma ratio)	3
Hartmann layer—analytical	4

tions are also expressed implicitly for higher accuracy in time, a point implicit relaxation strategy for time advancement would seem to be adequate. CFL numbers computed based on cell face normal velocities and their corresponding length scales can be chosen quite large, and can in fact be varied as the solution progresses. We have used CFL number in the range of 2–5 still with stable results in various situations.

A relaxation factor may be applied to all elliptic solvers in order to accelerate the solution. Over-relaxation factors in the range of 1–2 can be used here, depending on the size and quality of the mesh. We have favored the range of relaxation factors between 1.7 and 1.9 and this has worked well for all cases studied.

The relaxation technique to converge the pressure Poisson equation can be easily improved by better iterative techniques from linear algebra. Among the most popular methods to solve Poisson type equations without storing a coefficient matrix, is the conjugate gradient technique, where successive approximations are made to a matrix equation representing the discrete Poisson equation. These approximations are refined in order to minimize an error functional. The process converges rapidly, and there are many variants in the literature that improve upon the basic procedure and make changes based on prior knowledge of the nature of solutions to seek. The method has been implemented for HIMAG for scalar calculation but has not yet been extended to the parallel version.

HIMAG has inherited the parallel message passing environment from HyPerComp's suite of electromagnetics codes. Within each physical phase of the solution process, sub-iterations are performed and data is exchanged periodically across computer node boundaries. In Poisson solvers, such as pressure and potential, data may be exchanged only every 10 steps or so, to reduce the communication overhead in the starting stages of solution.

3.1.5. Computational parameters

HIMAG expects to address a wide multi-physical parameter space. The numerical algorithm treats both the advection and viscous terms implicitly, thereby allowing for strong variations in these terms. Liquid metal MHD computations are often restricted by the large values of the Hartmann number and the interaction parameter ($N = Ha^2/Re$) that are encountered. With our present approach, using an appropriate mesh resolution, we are able to run Hartmann numbers up to 10,000 with an interaction parameter of 1000 corresponding to a Reynolds number of 10^5 . At higher Hartmann numbers, even in simple geometries, a large number of mesh points are often needed, to resolve the Hartmann layers accurately. This number could run into several millions, depending on the linear dimensions of the geometry. The use of parallel computing is inevitable in such cases, where single processor runs are practically impossible. HIMAG has shown good scalability on parallel processors and has been tested successfully, to date, on PC clusters running LINUX. We have used Weber numbers in the range of 0.1–10 successfully, and density

ratios of about 1000 and higher in free surface flow calculations.

3.2. Code validation and benchmark problems

A code this complicated, with so many different features and capabilities, must be thoroughly benchmarked against existing analytic solutions and results of other codes and experiments in order to establish the accuracy of the numerical solutions and aid in the debugging process. A number of such benchmark cases are briefly reported here and are presented in more detail in [24].

3.2.1. 2D ordinary hydrodynamic flow

Perhaps the simplest code-verification strategy for incompressible Navier–Stokes solvers is to predict the pressure drop in a 2D channel with a fully developed parabolic velocity profile given as an initial condition. For a channel of unit width, and a peak velocity of 1, this gives a velocity distribution: $u = 4y(1 - y)$ and a $dp/dx = -8\mu$. The pressure profiles along the channel for the two cases of $Re = 50$ and 500 were calculated with HIMAG and exact pressure drop emerges easily from the numerical solution.

3.2.1.1. 2D driven cavity problem. A benchmark problem frequently used for incompressible solvers is the lid-driven cavity problem at $Re = 1000$. Here, a velocity of $u = 1$ is applied to the $y = 1$ face of a unit square, where all internal points are initially at rest. 2D problems are simulated in HIMAG by using one cell in the third (z -direction,) and selecting the boundary conditions on the z -facing boundaries to be “undefined”. A relatively uniform mesh and a severely stretched unstructured triangular mesh have been used in this study to test the effect of mesh skewness on the accuracy of the solution. Good solution convergence has been observed in both cases, with an insignificant residual divergence of the velocity. Various Poisson solver strategies have been experimented for this case, and it has been observed that the relaxation solver and the conjugate gradient techniques are both well suited for this purpose, with the CG technique being overall superior in terms of convergence rate and error reduction. Velocity vectors and streamlines for the two meshes are almost identical and the profiles match well with published data [39].

3.2.1.2. Backward facing step. The re-attachment point location of the flow entering a backward facing step has also been used for validation of spatial accuracy of the solver. A Reynolds number is computed from the average velocity of the inflow and using the channel half-width as the characteristic length scale. The re-attachment point location of $x/h = 5.2$ for $Re = 200$ and $x/h = 1.95$ for $Re = 160$ match closely with experimental and other CFD data in the literature [40].

3.2.1.3. 2D von Karman vortex street. The flow past a cylinder in 2D is known to become unsteady after a Reynolds number of about 41 (Re based on the diameter of the cylinder.) Such flows produce an oscillatory wake, in which rows of positive and negative vortices shed from the top and bottom of the cylinder alternately, propagate downstream. This is referred to as the *von Karman vortex street*. Experimenting with various meshes shows good comparison for dimensionless frequency to within 1% error of the published data [41], even with relatively coarse meshes.

3.2.1.4. 2D open-channel flow on an inclined plane. Including now the coupling to the level-set free surface tracking routines, a simple open-channel flow case is calculated. Among the various tests of merit of a free surface capture scheme is the sensitivity to mesh skewness, the tangency of the surface streamline under various density and viscosity ratios, and sensitivity to Weber and Froude numbers in the flow. We have found HIMAG to be fairly robust with regard to these concerns and close agreement between existing 2D and 3D codes is observed.

3.2.2. 2D MHD flows

Since the ordinary hydrodynamic solver appears to be accurate when compared to standard benchmark problems, these cases are expanded to include MHD effects to investigate the accuracy of the coupled electromagnetics and hydrodynamics solvers.

3.2.2.1. 2D axisymmetric open-channel flow in a gradient toroidal field. A validation case was selected for 2D free surface flow with MHD with the following specifications. A semi-parabolic inflow velocity profile with 0.1 m/s average velocity is given to a liquid flowing down an incline of 5° . A toroidal magnetic field was applied with a Gaussian profile $B_z =$

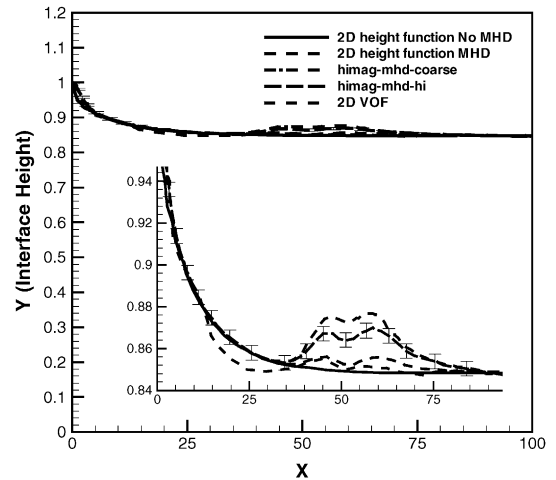


Fig. 11. Comparison of HIMAG to 2D axisymmetric codes for 2D free surface benchmark problem.

$0.5 \exp[-0.01(x/h_o - 50)^2]$ T, with the walls assumed to be electrically insulating. This is an axisymmetric problem that has been modeled by the various 2D codes described in the Section 2. A double bump in the free surface shape is observed corresponding to the rise and fall of the Gaussian magnetic field distribution.

This problem was modeled in HIMAG using two fluids of density, viscosity and electrical conductivity ratio of 1000 between the heavier and lighter fluid. Many different grids were tested for the test case with HIMAG, where a non-dimensional domain size of 100×1.5 was chosen. The 2D-VOF simulation used a mesh of 1000×500 equally spaced cells, with channel size of 100×2 . The 2D height function code used 201×101 grids with channel size of 100×1 . Error bars have been placed on the HIMAG result shown in Fig. 11, corresponding to the mesh resolution at the free surface. The results seem to agree within 1% tolerance, and the differences are believed to be due to differences between the various formulations (the benchmark result uses a B-formulation). A new benchmark problem with a stronger gradient has been proposed in order to cause a larger deviation from the base flow, but data on this new problem is not yet available.

3.2.3. 3D MHD flows in closed channels

It is difficult to find benchmark problems for fully 3D MHD flow with free surfaces, in fact none exist to our knowledge. To have some 3D benchmark data,

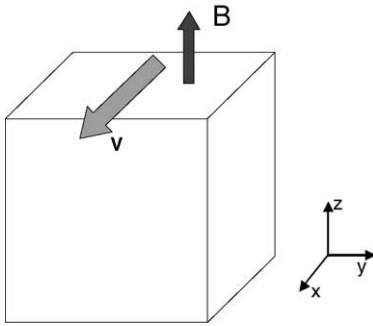


Fig. 12. Geometry of 3D driven cavity benchmark problem.

then, two closed-channel flows are calculated for which there is some existing data.

3.2.3.1. 3D lid driven cavity. Similar to the 2D driven cavity, a 3D driven cavity problem was prepared in a unit cube with magnetic field perpendicular to the moving wall as shown in Fig. 12. For comparison to HIMAG two other 3D codes (called simply code 1 and code 2) were developed specifically for this geometry using structured grids. Also, the calculations were performed using the commercial CFD software package FLUENT [42] using a new limited MHD module currently being developed by FLUENT.

Code 1 solves the governing equations by finite difference approximation using a fully staggered grid system in which each variable is defined at a different location. The pressure is located in the cell center and the velocities are in the centers of the corresponding sides. The components of the induced magnetic field are shifted from the velocity locations by half of the grid size in the Z-direction. Such a grid arrangement allows for a compact evaluation of both the Lorentz force term on the RHS of the momentum equation and the velocity containing terms on the RHS of the induction equation, so that averages of \mathbf{V} and \mathbf{B}^i are not required. The continuity equation is discretized at the center of the cell. The projections of the momentum equations and those of the induction equation are discretized at points where the corresponding variables are defined. As a discretization scheme for the convective terms, a mixture of the central difference approximation and the donor-cell discretization is used. The time-advancing step consists of two sub-steps. First, the provisional velocity field is calculated from the momentum equation

in which the pressure gradient terms are omitted. The Lorentz force terms in the momentum equation are also calculated in the first sub-step by solving the induction equation and then using ampere's law. In the second sub-step, the provisional velocity is corrected by accounting for the pressure gradient and the continuity equation through solving the pressure Poisson equation. The approach developed belongs to the group of explicit projection methods and is similar to that proposed in [43] and [44] for non-MHD flows. The pressure Poisson equation is solved at each time step by SOR method. The induction equation is approximated with a conservative scheme analogous to that in [45] so that the conjugation conditions across the boundaries of the flow domain are directly satisfied. The code developed was verified by comparison with the non-MHD results calculated in [46] with the vorticity-velocity approach.

Code 2 is an adaptation of existing cell-centered code [47] where a general four-step and three-step projection method has been developed for incompressible Navier–Stokes equation. This general projection method has been further extended to solve a modified induced magnetic equation with a penalty function ∇q [48] added to aid in enforcing $\nabla \cdot \mathbf{B}^i = 0$. The projection methods for induced magnetic field equation can ensure the divergence of induced magnetic field zero (for the case of 3D lid-driven cavity flow, we have the divergence of induced magnetic field as 10^{-14}) without employing special grid arrangement. Hence it can be easily extended to an unstructured grid system. In the soon future, this developed projection method will be applied on HIMAG for the higher Hartmann number cases.

Results from HIMAG and other models and experiments seem to agree well for the cases studied, while presenting slight differences in the treatment of electromagnetic fields. Various cuts of the velocity profile are shown in Fig. 13 demonstrating the level of agreement.

3.2.3.2. 3D developing flow in a channel. A case studied by Sterl [49] has been utilized to test 3D MHD models in HIMAG (see Fig. 14). A channel of unit square cross-section of dimensionless length -4 to 4 with prescribed inlet velocity $u(y, z) = (9/4)(1 - y^2)(1 - z^2)$ is studied under the influence of an applied magnetic field of the form $B_y = 1/(1 + \exp[-x/0.15])$ which has strong variation near $x = 0$.

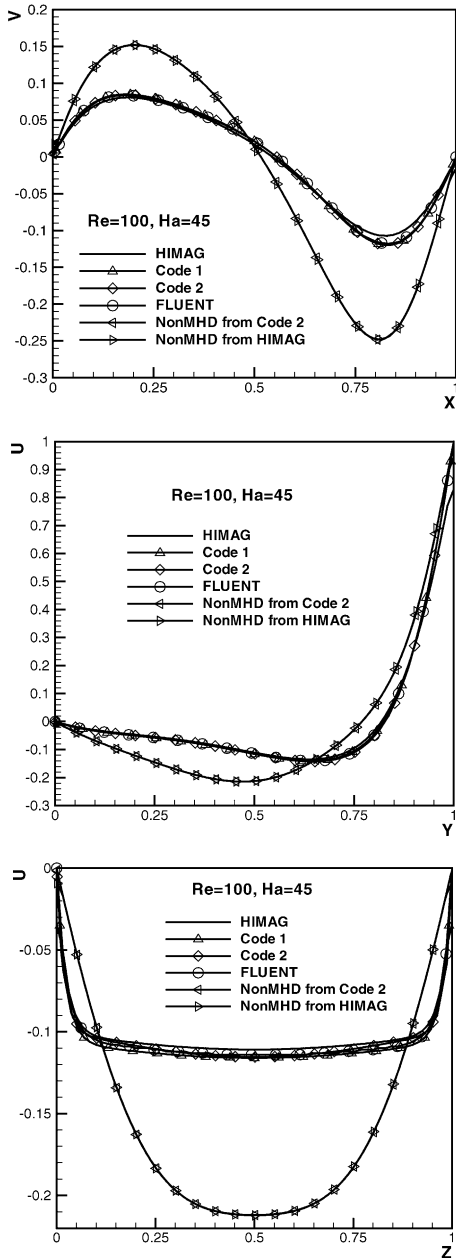


Fig. 13. Comparison of velocity profiles in 3D driven cavity problem for $Re = 100$, $Ha = 45$.

This case was studied for the Hartmann numbers of 50, 200 and 1000. A highly stretched rectangular mesh was used here, taking care to resolve the Hartmann layers and wall jets appropriately, without a prohibitively

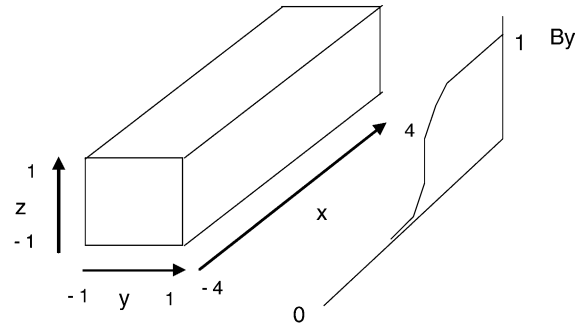


Fig. 14. Channel geometry and test conditions for 3D MHD benchmark problem.

large number of mesh points. It is observed following the increase in magnetic field strength, or, alternatively, the Hartmann number, that flow physics change significantly. Wall jets are formed, that contain most of the mass flow, while sharp Hartmann layers are formed at the walls perpendicular to these jets. The effect gets progressively larger, until when the core of the flow loses all of its momentum and forms a re-circulating vortex core. At this point, a trailing wake system appears, and begins to slowly flutter at a frequency which we did not measure in this particular study.

In all of the numerical simulations, the non-dimensional interaction parameter $N = (Ha^2/Re)$ was kept fixed at 1000. Fig. 15 shows the pressure variation at the center line of the channel for $Ha = 50$ and 200. The slope of the pressure profile from fully developed channel flow results is shown alongside for comparison. Fig. 16 shows a sampling of the 3D velocity profiles at different axial locations. The development of the expected M-shaped velocity profiles and Hartmann layers for high Hartmann number are easily seen. With the highly stretched mesh used here, it has been possible to simulate Hartmann numbers of up to 1000 without any special procedures for stability.

For the purpose of validation, results from a code that solves the fully developed closed channel MHD flows in ducts [50] were used. The comparison with fully developed flow is only valid when the flow becomes uniform in the axial direction, and may not occur (to engineering precision) within the channel length considered here for an arbitrarily flow and electromagnetic conditions. The fully developed flow results are thus, used as guidelines in estimating the approximate validity of the numerical solution. Fig. 17 shows the

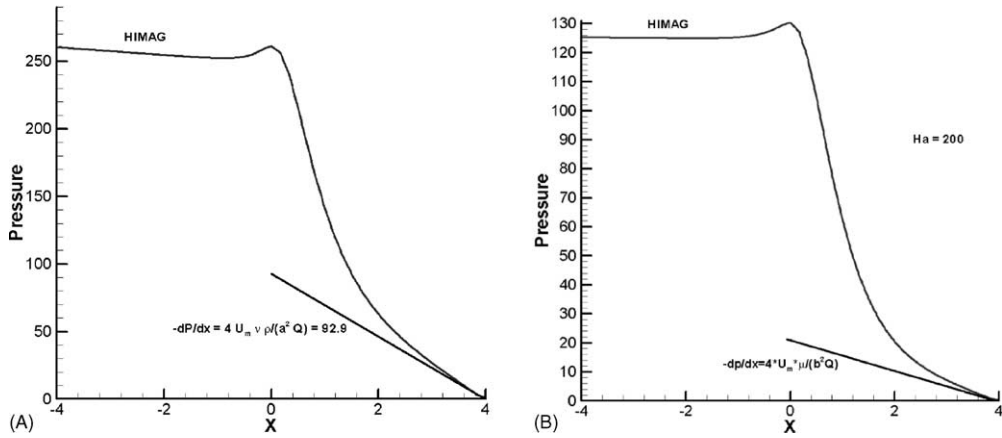


Fig. 15. Comparison of fully developed pressure gradient calculation with the developing channel flow computation from HIMAG with (A) $Ha = 50$ (B), $Ha = 200$.

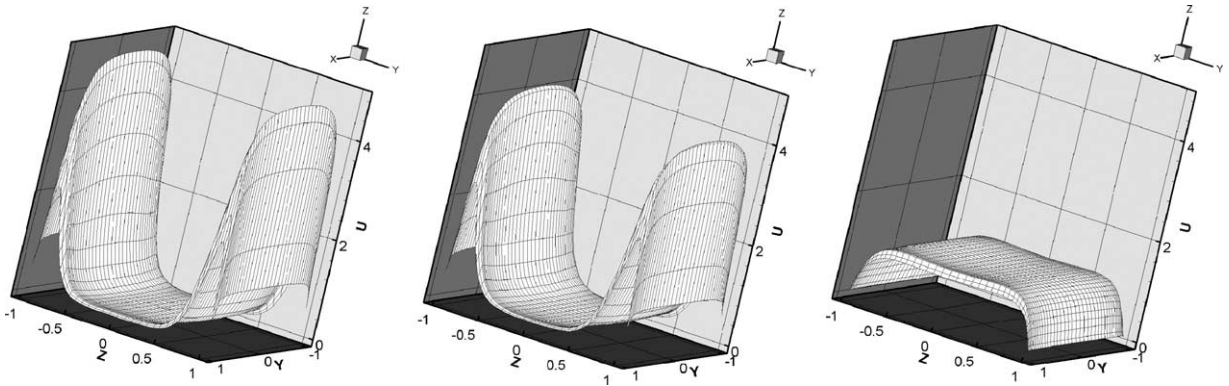


Fig. 16. $Ha = 200$, $N = 1000$, velocity profiles at various downstream locations following the steep magnetic field gradient at $x = 0$.

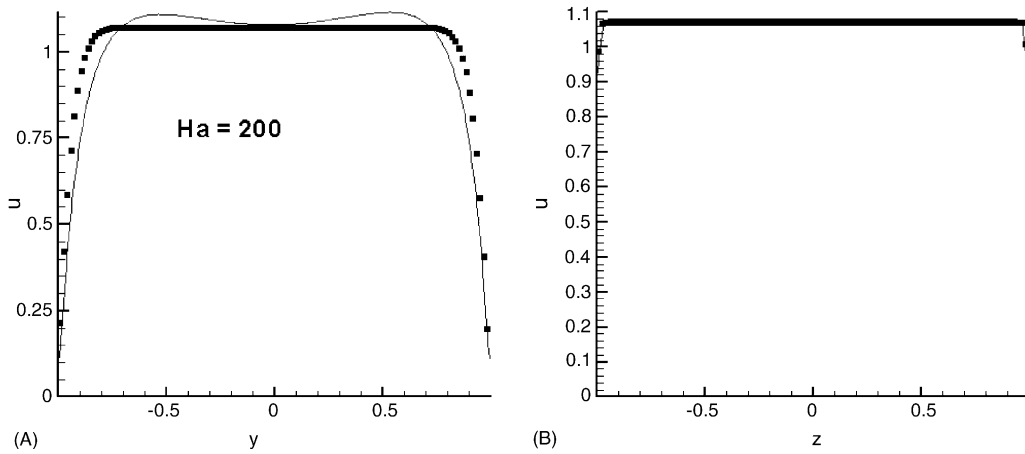


Fig. 17. Comparison of fully developed velocity profile (symbols) with 3D solution from HIMAG at the exit plane, u -velocity on the center lines.

favorable comparison of fully developed profile to the HIMAG results near the exit plane. Sterl [49] validates 3D effects of the developing flows by comparing with fully developed flow results. Very little has been said about insulating walls in the above paper. However, Table 1 on p. 184 mentions the maximum transverse variations in the electric potential, pressure and the moment-center of the velocity distribution at the location $x = 0$. These results are in good agreement with the results from HIMAG (e.g. the value of $\Delta\phi = 1.01$ computed from HIMAG, while Sterl gives 1.0390—this result is scaled by the Hartmann number and is essentially independent of it).

3.2.4. Parallel code execution benchmarks

HIMAG can be run in parallel across multiple processors. Message passing interface (MPI), a freely available and widely employed software suite, is used for parallel communications. Presented here are some preliminary results and scaling studies. HIMAG performance was tested on three types of calculations to assess the time taken by each. The same computational mesh, of $60 \times 60 \times 100$ cells was used in a rectangular domain of size $1 \times 1 \times 5$ in all three cases. The three cases were:

- impulsively started single phase flow;
- two-phase flow with bi-parabolic initial velocity;
- single phase flow with MHD.

The mesh was first partitioned into 2, 4 and 16 partitions as seen in Fig. 18.

The impulsive flow initial condition is useful in assessing the stability of the numerical procedure. Fully developed initial velocity profiles normally are much more stable, but it was found that the solution converged well even for the impulsive start, thus indicating that the code is well behaved even in the parallel mode to fluid kinetic parameters. A bi-parabolic velocity profile was used for the two phase flow case with density and viscosity ratio of 1000. The flow was seen to converge smoothly, with streamlines tangential to the free surface at convergence (a very desirable property).

Scaling studies were made for cases run with 2, 4 and 16 processors assuming a fixed number of the pressure Poisson equation and the level set reinitialization steps were used. For a time accurate calculation, it may be hard to specify the number of steps, and may be simpler to use a tolerance level. It is seen in Fig. 19 that nearly

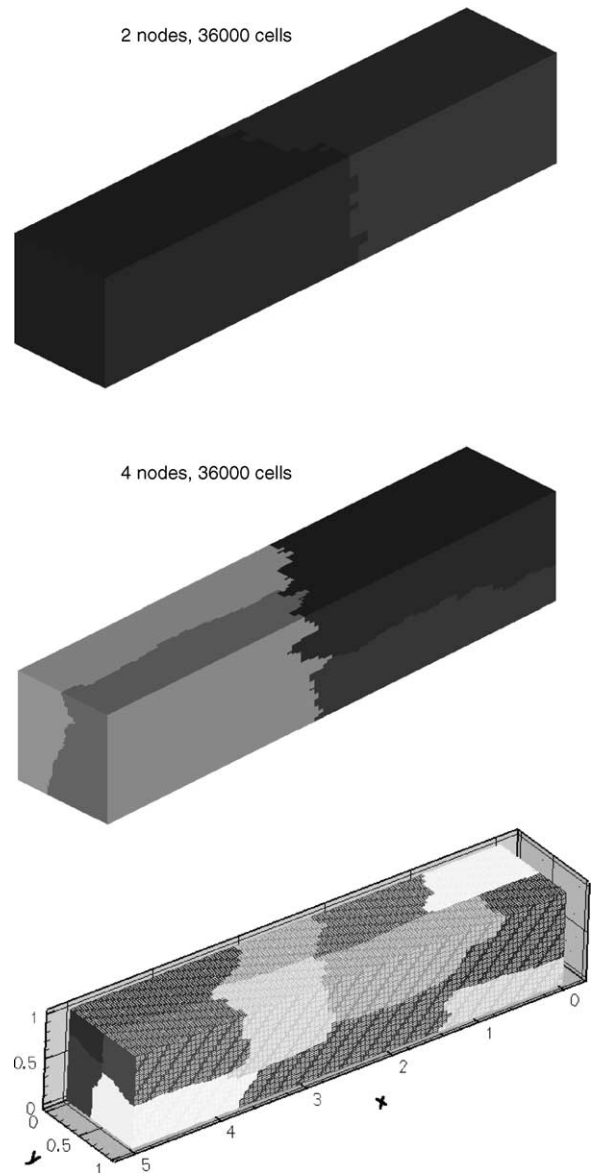


Fig. 18. Sample domain partitioning for a channel geometry with 360,000 cells using 2, 4 and 16 (left) partitions.

linear performance was obtained for the single-phase flow, with an efficiency of about 95%. With two-phase flow, the efficiency dropped a little, to 91%, and with MHD, the efficiency returned to close to 96%. These numbers are highly encouraging from the perspective of parallelization. The relative time consumed by the level set solver and MHD may be estimated from the

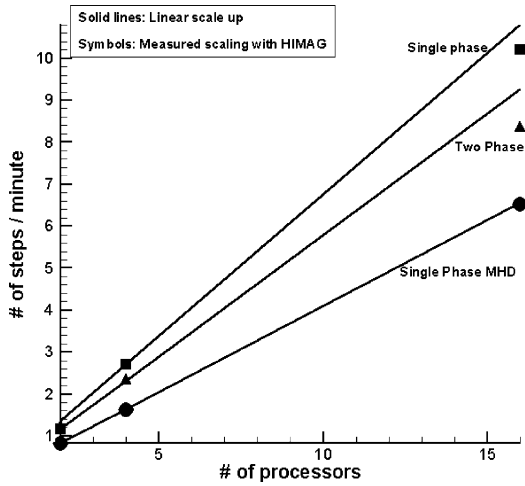


Fig. 19. Parallel performance of HIMAG for a single phase channel flow, two phase flow, and MHD channel flow.

drop in performance from the single-phase solver for these two cases.

3.3. Fusion relevant test problems

While the HIMAG code has just recently neared the production stage, there has been a great interest in the

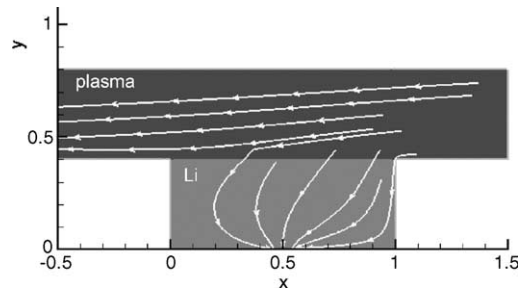


Fig. 21. Current streamlines for $z = 0$ cross-section at $t \approx 0$ given a 40 kA/m^2 inlet plasma current.

APEX community to simulate different real problems to help in the understanding of phenomena observed in experimental tests currently underway. Three such problems are addressed below.

3.3.1. Simulation of liquid lithium motion in DiMES sample holder in DIII-D

Here, we simulate the plasma-current driven MHD flow in an initially static lithium pool with geometry (see Fig. 20) and plasma current as proposed for a new lithium experiment in Diverter Materials Evaluation System (DiMES) probe apparatus in the DIII-

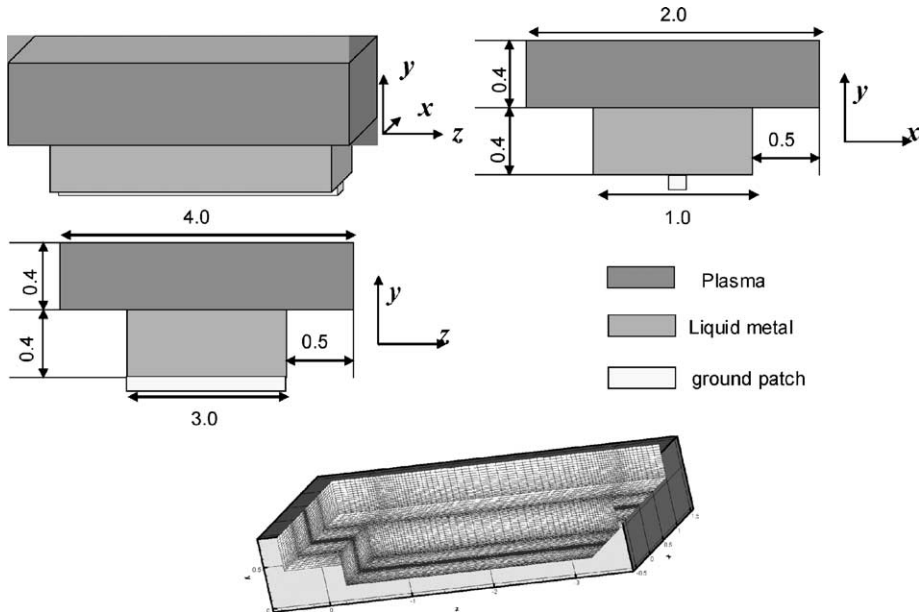


Fig. 20. Sketch of the new DiMES probe slot geometry and HIMAG numerical grid.

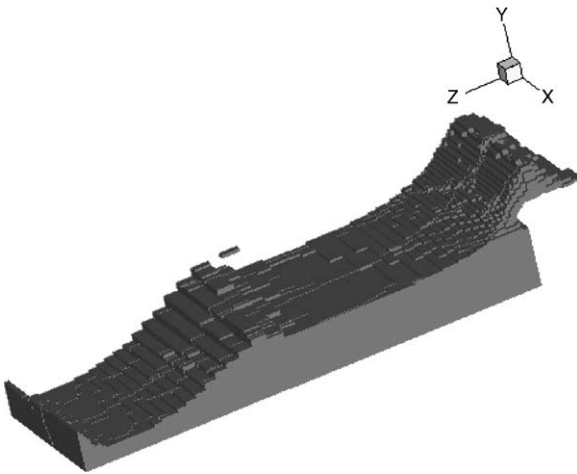


Fig. 22. 3D view of the liquid lithium surface in DiMES slot after $t = 3.5$ ms with 40 kA/m^2 plasma current.

D tokamak facility [51]. The static pool is placed in contact with the divertor plasma where currents are expected to close through the liquid, causing MHD forces.

In this slot geometry, the lower block contains the liquid metal, and is made of insulating material, but for the thin strip of conducting material that is grounded at zero potential. Plasma current with density 40 kA/m^2 enters the domain at the far right edge of the upper block in the x -direction at an inclination of 3° to the horizontal, parallel to the 2 T magnetic field. The upper block is initially comprised of plasma, where the electrical conductivity is greater in the direction of the magnetic field than in the directional perpendicular to it. The electrical conductivity of the plasma is held at 1000 times less than that of the isotropic liquid metal, and so the current lines close to liquid surface, therefore, seek the low resistance path to the grounding plate at the lower wall. Fig. 21 depicts a 2D slice of the DiMES geometry with the computed electric current paths shown.

Several simulations (see Fig. 22) of liquid-metal flows in this geometry were made, with the liquid metal initially at rest. Several qualitative features of the solution were verified including the tendency of the liquid to push out of the sample holder seen in preliminary DiMES experiments.

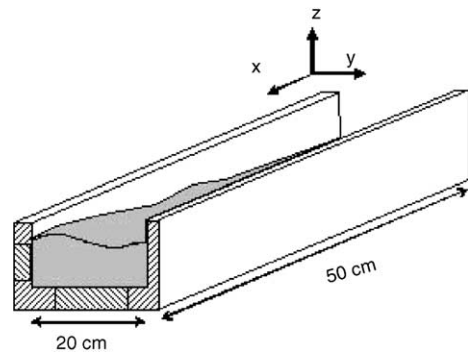


Fig. 23. MTOR quasi-2D test channel geometry.

3.3.2. Quasi-2D channel experiment in MTOR

The flow of liquid metal in an open-channel with geometry (see Fig. 23) and field similar to an experiment with liquid gallium alloy in the UCLA MTOR facility [14] was simulated and compared against experimental results. In the case selected (see Table 3), the magnetic interaction parameter was fairly low, and the flow is dominated by viscous and advective effects, except that flow laminarization by the magnetic field is expected. The magnetic field profile is $B_y = 0.45/(1+2x) \text{ T}$ as a function of the flow direction coordinate.

The experiment has a large aspect ratio so that 2D models could be compared against the experimental data. HIMAG was used to simulate this same case in 2D and 3D. A mesh resolution study first revealed the need for clustering mesh points close to the Hartmann walls, where Hartmann layers were seen to form. A rather finely clustered mesh was generated, using the number $1/Ha$ (where Ha is the Hartmann number based on the width of the channel,) as the non-dimensional

Table 3

Parameters of the quasi-2D open channel MHD benchmark problem and Ga–In–Sn alloy in MTOR facility

Volumetric flowrate (l/s)	0.26
Initial depth (mm)	2
Channel width (cm)	20
Initial average velocity (m/s)	0.65
Viscosity (m^2/s)	4.4×10^{-7}
Electrical conductivity (Ω/m)	3×10^6
Surface tension (N/m)	0.55
Density (kg/m^3)	6333

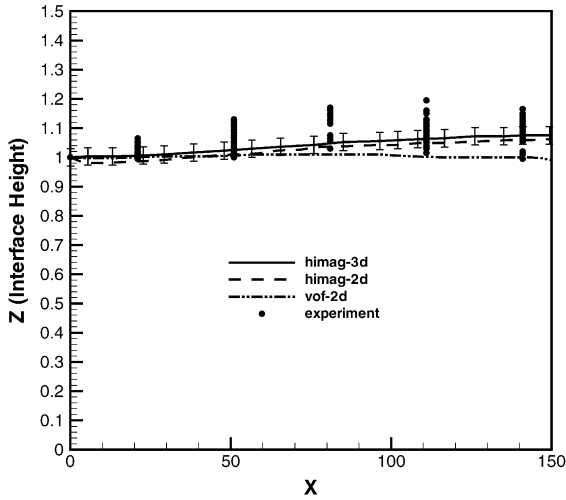


Fig. 24. MTOR data compared to 2D and 3D MHD solutions for the parameters given in Table 2. Spread of experimental data due to wave phenomena not resolved in the numerical calculations.

distance from the wall that had to be resolved. A total of 200,000 computational cells were present in this mesh.

Computed results for free surface height compared to averaged MTOR data are shown in Fig. 24 and seem to match closely, with better accuracy than the 2D axisymmetric model. The code was able to resolve wavy patterns emerging from the Hartmann walls as part of the captured free surface seen in Fig. 25.

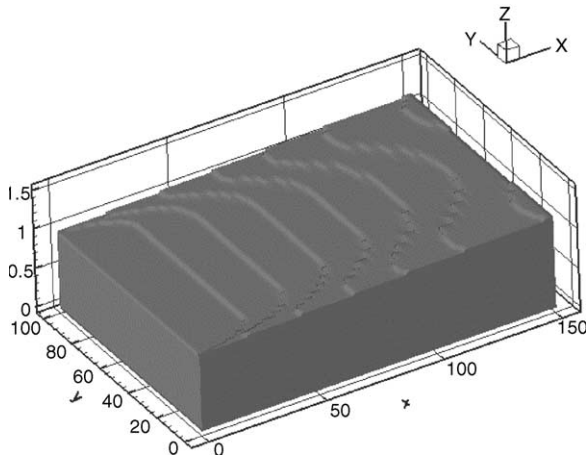


Fig. 25. 3D image of gallium surface from HIMAG calculation for the MTOR parameters in Table 2 at steady state.

3.3.3. NSTX simulation experiment in MTOR

In this simulation a liquid metal film flows from a nozzle with electrically conducting walls out into a channel, also with conducting side walls, with a spatially varying multiple component magnetic field is modeled. Fig. 26 shows a dimensioned sketch of this flow geometry. The liquid metal used in the MTOR experiment this test problem is attempting to simulate is the same gallium alloy as described in Table 3. The channel walls were made of 304 stainless steel. A flow speed of about 3 m/s at the nozzle exit was estimated.

This complex geometry, multi-material case serves as a test of all the features of the HIMAG code (except heat transfer). The computational mesh for this problem was prepared, with the appropriate modifications to include solid walls. Fig. 26B shows a view of this mesh, containing 327,744 cells and 311,690 nodes. Solid walls were defined in the mesh generator. The computational run was initiated using an impulsive start of the flow. That is, velocity is initially set to zero everywhere inside the domain, and an inflow velocity is applied at time $t = 0$. Such an initialization is often problematic, since it poses numerical stability problems. However, with suitably converged pressure Poisson solver, it was possible to implement it into the code easily.

Preliminary results from the MHD simulation of this case show clearly, the evolution of smooth pressure and electric potential contours (Fig. 27). Current vectors entering solid walls and forming closed pathways inside the solid medium have been observed. Fig. 28A and B show the flow of current prior to nozzle exit. Aft of the nozzle exit, the upper wall that had provided the closed circuit for current flow, is absent, and current begins to flow along the x -direction in the solid walls. This is seen in Fig. 28C. Fig. 28D shows the velocity vectors in the flow as it exits the nozzle. Detailed studies of this problem are presently underway and not yet ready for publication.

4. Conclusions and future directions

The modeling capabilities for simulating free surface LM-MHD flow have evolved greatly over the past two years of research and development within the APEX project. Various 2D and 3D capabilities have

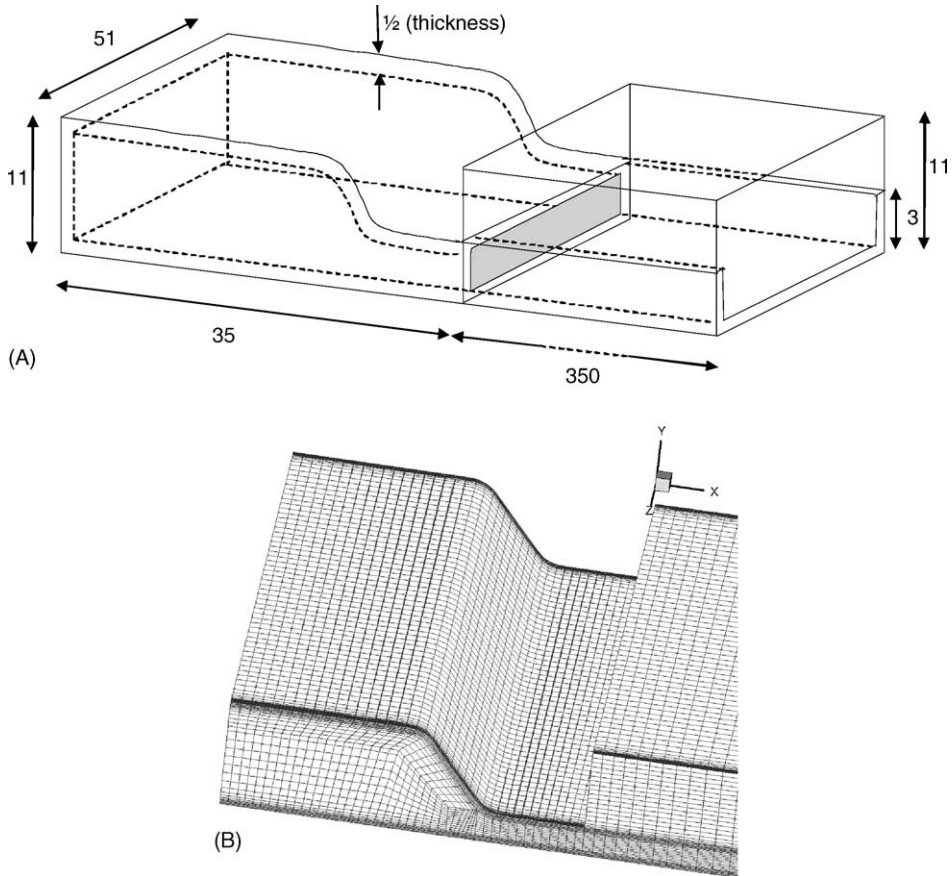


Fig. 26. NSTX film flow experiment geometry in MTOR. (A) Isometric view of the geometry (note to scale—all dimensions in mm), (B) a portion of the numerical grid in the nozzle region and (C) viscosity contours, showing solid (304 SS) walls.

been developed and a great deal has been learned about the hydrodynamics of liquid walls. Field gradients typical of the large toroidal magnetic field have been shown to have only small effect on the drag for thin ($\sim <2$ cm) liquid wall flows, but still may have detrimental effects

on the surface stability especially for lithium flowing on conducting surfaces. The magnetic propulsion concept has been shown to be effective in propelling and stabilizing liquid walls flowing from strong to weak field regions. This concept might be especially useful in

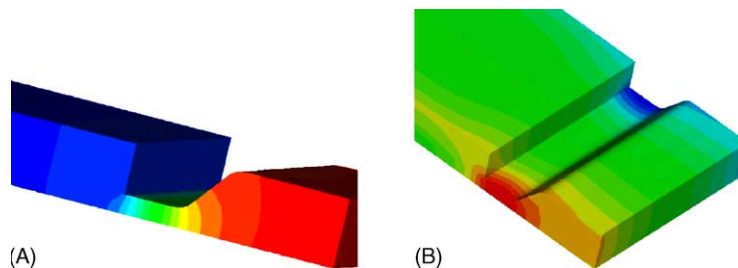


Fig. 27. (A) Pressure distribution, and (B) electrical potential distribution in the near nozzle region at steady state.

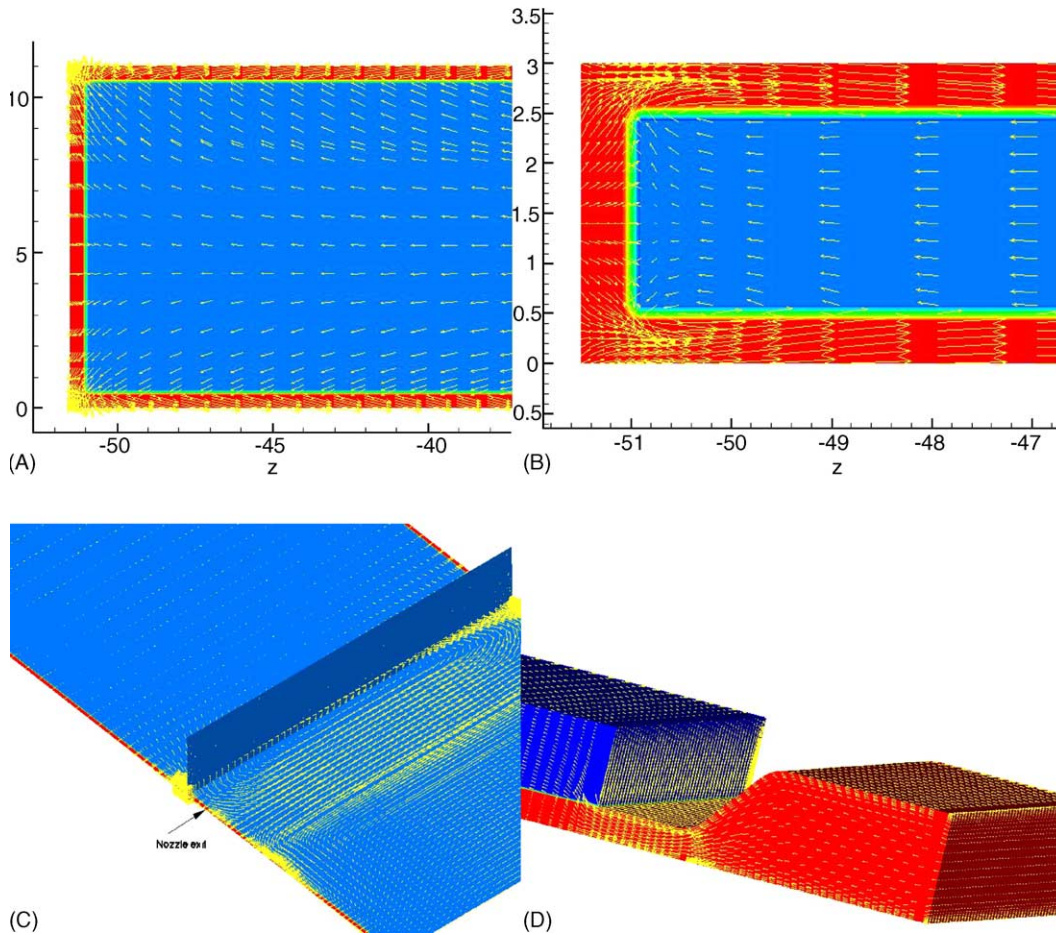


Fig. 28. Current vectors in (A) $x = 6$ mm plane inside the nozzle, (B) $x = 35$ mm plane at the nozzle exit, (C) in x - z and y - z planes, (D) velocity vectors at nozzle exit.

forces liquid out through drain channels between magnetic field coils. Multiple component magnetic fields lead to more complicated effects, most notably strong toroidal motion in liquid wall flows that are initially flowing poloidally. The impact of this toroidal flow on the concept of using sector dividing walls may be very serious.

In terms of new numerical capability and technique, the HIMAG 3D code is poised to push the boundaries of computational magnetohydrodynamics even further in the flow parameters and geometries that can be simulated. Several complex geometry/field cases have been described above as examples of the simulation possibilities that HIMAG can address—but no conclusions have been reached regarding some the complex geome-

try features of liquid wall designs such as penetrations, sidewalls, fins and deflectors as this capability is just now becoming available.

Work still needs to continue on various R&D tasks that are essential to the further understanding and prediction of liquid walls. Despite the headway made, there remains critical work remaining in some areas of HIMAG development and detailed application to problems of interest to liquid walls that should continue to be pursued. These include, importantly:

- (a) an implicit treatment of level set equations at high order of accuracy;
- (b) boundary element method for semi-infinite and closed surfaces in the flow;

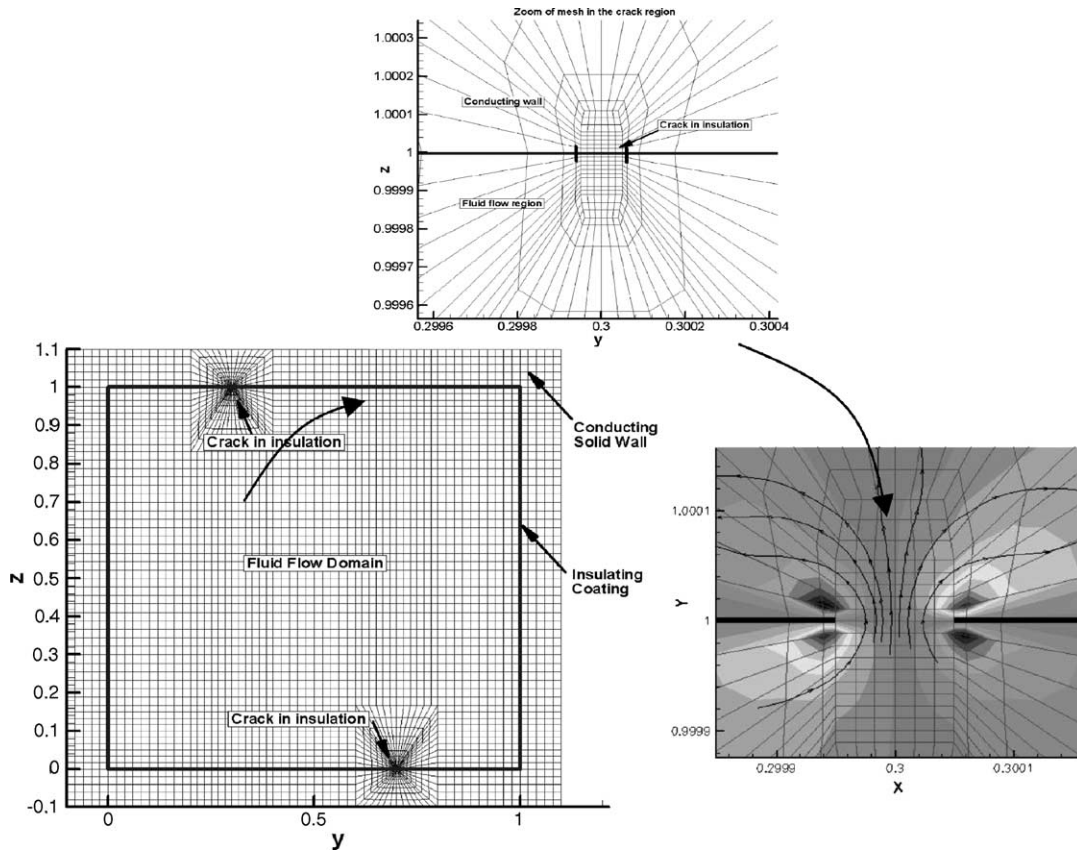


Fig. 29. Section of a channel flow with fine (10^{-5} of channel dimension) crack, resolved economically using unstructured hexahedral mesh. Sample contour plot of x -current density and current lines are shown.

- (c) induced magnetic field and vector potential EM formulations to help push high Hartmann number and magnetic Reynolds number;
- (d) continued validation and application for various MHD flows of engineering importance—for instance closed channel MHD flows with insulator coating imperfections.

Referring to this last bullet, some preliminary work has already been performed to assess the capabilities of HIMAG for closed channel flows with multiple materials having various electrical conductivity. Fig. 29 shows a sample situation where the true power of unstructured meshing in HIMAG can be demonstrated. Currents emerging from a conducting channel (cross-section of which is shown,) may flow into the conducting exterior wall through two cracks in the insulating medium that separates the two. The size of

the cracks is very small (five orders of magnitude less than channel dimensions). With a typical structured mesh, many mesh cells will be wasted in resolving this crack dimension, since the mesh lines will have to extend across the channel. Unstructured meshes enable this computation to be performed with only local clustering. It is believed that this framework may be extended more generally to 3D problems to study the effectiveness of insulation coatings. Work has been also proposed to add various turbulent and conjugate heat transfer effects to HIMAG in future years, and magnetic formulations that can extend the magnetic parameter ranges reachable by numerical simulation. With these capabilities, HIMAG will have the potential to serve as a true design tool for fusion reactor design, as well as other applications in metallurgy and aerospace propulsion involving multi-phase MHD.

Acknowledgements

This work was supported by U.S. Department of Energy grants #DE-FG03-86ER52123 and #DE-FG03-00ER83018. The authors would like to acknowledge the APEX team members and Sam Berk of the Department of Energy. Their hard work and innovative spirit have contributed greatly to this work.

References

- [1] M.A. Abdou, A. Ying, N.B. Morley, et al., On the exploration of innovative concepts for fusion chamber technology, APEX Interim Report, UCLA-ENG-99-206, UCLA-FNT-107, November 1999.
- [2] M.A. Abdou, A. Ying, N. Morley, et al., On the exploration of innovative concepts for fusion chamber technology, APEX Interim Report Overview, Fusion Eng. Des. 54 (2001) 181–247.
- [3] N.B. Morley, S. Smolentsev, D. Gao, Modeling infinite/axisymmetric liquid metal magnetohydrodynamic free surface flows, Fusion Eng. Des. 63–64 (2002) 343–351.
- [4] D. Gao, N. Morley, M. Abdou, V. Dhir, Numerical study of stability of liquid metal falling film flows in a varying spanwise magnetic field, Fusion Eng. Des. 64 (2002) 369–374.
- [5] D. Gao, N.B. Morley, Equilibrium and initial linear stability analysis of liquid metal falling film flows in a varying spanwise magnetic field, Magnetohydrodynamics 38 (4) (2002) 359–375.
- [6] D. Gao, N.B. Morley, V. Dhir, Surface wave behaviors in a magnetic field gradient obtained by numerical simulation, UCLA Report No. UCLA-FNT-205, 2004.
- [7] D. Gao, N.B. Morley, Numerical investigation of surface disturbance on liquid metal falling film flows in a magnetic field gradient, Magnetohydrodynamics 40 (2004).
- [8] S. Smolentsev, M. Abdou, T. Kunugi, N. Morley, S. Satake, A. Ying, Modeling of liquid wall flows in APEX study, J. Appl. Electromagn. 13 (2001/2002) 373–379.
- [9] L.E. Zakharov, Magnetic propulsion of intense lithium streams in a tokamak magnetic field, Phys. Rev. Lett. 90 (4) (2003) 045001/1–4.
- [10] S. Smolentsev, M. Abdou, Open-surface MHD flow over a curved wall in the 3-D thin-shear-layer approximation, UCLA Report No. UCLA-FNT-204, 2004.
- [11] F.G. Blottner, Variable grid scheme applied to turbulent boundary layers, Comput. Meth. Appl. Mech. Eng. 4 (1974) 179–194.
- [12] B.D. Nichols, C.W. Hirt, Calculating three-dimensional free surface flows in the vicinity of submerged and exposed structures, J. Comput. Phys. 12 (1973) 234–246.
- [13] S. Smolentsev, M. Abdou, N. Morley, A. Ying, T. Kunugi, Application of the “ $K-\epsilon$ ” model to open channel flows in a magnetic field, Int. J. Eng. Sci. 40 (2002) 693–711.
- [14] N.B. Morley, J. Burris, The MTOR LM-MHD flow facility, and preliminary experimental investigation of thin layer, liquid metal flow in a $1/R$ toroidal magnetic field, Fusion Technol. 44 (1) (2003) 74–78.
- [15] S. Smolentsev, Unsteady magnetohydrodynamic flows under a non-uniform magnetic field, UCLA Report No. UCLA-FNT-203, 2004.
- [16] J.C. Tannehill, D.A. Anderson, R.H. Pletcher, Computational Fluid Mechanics and Heat Transfer, 2nd ed., Taylor & Francis, 1997.
- [17] A. Samarskii, Introduction to the Theory of Finite-Difference Schemes, Moscow, Nauka, 1971 (in Russian).
- [18] E.G. Puckett, A.S. Almgren, J.B. Bell, et al., A high-order projection method for tracking fluid interfaces in variable density incompressible flows, J. Comput. Phys. 130 (1997) 269–282.
- [19] J.U. Brackbill, D.B. Kothe, C. Zemach, A continuum method for modeling surface tension, J. Comput. Phys. 100 (1992) 335–354.
- [20] D. Gao, N.B. Morley, V. Dhir, Numerical simulation of wavy falling film flows using VOF method, J. Comput. Phys.
- [21] D. Gao, Numerical simulation of surface wave dynamics of liquid metal MHD flow on an inclined plane in a magnetic field with spatial variation, Ph.D. Dissertation, Mechanical Engineering Department, University of California Los Angeles, 2003.
- [22] H.L. Huang, A. Ying, M.A. Abdou, 3D-MHD free surface fluid flow simulation based on magnetic-field induction equations, Fusion Eng. Des. 63–64 (2002) 361–368.
- [23] X. Luo, A. Ying, M. Abdou, Experimental and computational simulation of free jet characteristics under transverse field gradients, Fusion Technol. 44 (1) (2003) 85–93.
- [24] R. Munipalli, et al., Development of a 3-D incompressible free surface MHD computational environment for arbitrary geometries: HIMAG, DOE SBIR Phase-II Final Report, June 2003.
- [25] V. Shankar, CFD-based higher order methods for broad band parallel applications in computational electromagnetics (CEM), ICCFD2, in: Proceedings of the Second International Conference on CFD, Sydney Australia, July 2002.
- [26] R. Munipalli, V. Shankar, Development of computational capabilities in real gas MHD simulations, AIAA paper 2001-0198, Presented at the 39th AIAA Aerospace Sciences Meeting & Exhibit, Reno, NV, January 2001.
- [27] S. Smolentsev, S. Cuevas, N. Morley, On the choice of variables in modeling liquid metal magnetohydrodynamic flows at low magnetic Reynolds number, UCLA Report No. UCLA-FNT-202, 2004.
- [28] S. Osher, R. Fedkiw, Level Set Methods and Dynamic Implicit Surfaces, Springer-Verlag, New York, 2003.
- [29] T. Nakata, N. Takahashi, K. Fujiwara, K. Muramatsu, Z.G. Cheng, Comparison of various methods for 3-D eddy current analysis, IEEE Trans. Magn. 24 (1988) 6.
- [30] B. Perot, An analysis of the fractional step method, J. Comput. Phys. 108 (1993) 51–58.
- [31] D. Kim, H. Choi, A second-order time-accurate finite volume method for unsteady incompressible flow on hybrid unstructured grids, J. Comput. Phys. 162 (2000) 411–428.
- [32] J. Van Kan, A second order accurate pressure-correction scheme for viscous incompressible flow, SIAM J. Sci. Comput. 7 (1986) 870–891.

- [33] M.-J. Ni, S. Komori, N. Morley, Projection methods for the calculations of incompressible unsteady flows, *Numer. Heat Transfer B* 44 (2003) 533–551.
- [34] M.-J. Ni, S. Komori, M. Abdou, A Variable density projection method for interfacial flows, *Numer. Heat Transfer B* 44 (2003) 553–574.
- [35] Y. Zang, R.L. Street, J.R. Koseff, A non-staggered grid, fractional step method for time-dependent incompressible Navier–Stokes equations in curvilinear coordinates, *J. Comput. Phys.* 114 (1994) 18–33.
- [36] E. Ruoy, A. Tourin, A viscosity solutions approach to shape from shading, *SIAM J. Numer. Anal.* 29 (3) (1992) 867–884.
- [37] T.J. Barth, Aspects of unstructured grids and finite volume solvers for the Euler and Navier–Stokes equations, von Karman Institute lecture series, Report 1994-05, 1994.
- [38] H. Jasak, Error analysis and estimation for the finite volume method with applications to fluid flows, Ph.D. Thesis, Imperial College, UK, June 1996.
- [39] U. Ghia, K.N. Ghia, C.T. Shin, High- Re solutions for incompressible flow using the Navier–Stokes equations and a multi-grid method, *J. Comput. Phys.* 48 (1982) 387.
- [40] B.F. Armaly, F. Durst, J.C.F. Pereira, B. Schonung, Experimental and theoretical investigation of backward-facing step flow, *J. Fluid Mech.* 127 (1983) 473.
- [41] C.H.K. Williamson, Oblique and parallel modes of vortex shedding in the wake of a circular cylinder at low Reynolds numbers, *J. Fluid Mech.* 206 (1989) 579.
- [42] FLUENT 6.0 User’s Guide, Fluent Inc., 2002.
- [43] A.J. Chorin, Numerical Solution of the Navier–Stokes Equations, *Math. Comput.* 22 (1968) 745–762.
- [44] R. Temam, Sur l’Approximation de la Solution des Equations de Navier–Stokes par la Methode des pas Fractionnaires, *Arch. Rational Mech. Anal.* 32 (1969) 135–153.
- [45] A. Samarskii, P. Vabishchevich, *Computational Heat Transfer*, vol. 2, Wiley, 1995, p. 421.
- [46] G. Gui, F. Stella, A vorticity-velocity method for the numerical solution of 3D incompressible flows, *J. Comput. Phys.* 106 (1993) 286–298.
- [47] M.-J. Ni, et al., A projection method for incompressible interfacial MHD flows, in: *Proceedings of the LANL Workshop on TELLURIDE at Santa Fe, NM, January 21–23, 2003*.
- [48] N. Ben Salah, A. Soulaïmani, W. Habashi, A finite element method for magnetohydrodynamics, *Comput. Meth. Appl. Mech. Eng.* 190 (2001) 5867–5892.
- [49] A. Sterl, Numerical simulation of liquid-metal MHD flows in rectangular ducts, *J. Fluid Mech.* 216 (1990) 161–191.
- [50] S. Smolentsev, A. Tananaev, Development of computer code for analysis of heat transfer in liquid metal MHD flows in ducts, *Magnetohydrodynamics* 31 (4) (1995) 414–419.
- [51] D.G. Whyte, T.E. Evans, C.P.C. Wong, W.P. West, R. Bastasz, J.P. Allain, J. Brooks, Experimental observations of lithium as a plasma-facing surface in the DIII-D tokamak divertor, *Fusion Eng. Des.*, this issue.